Mechanical Forces during Lymph Node Expansion Govern Fibroblastic Reticular Network Remodeling

Harry L. Horsnell[1], Robert J. Tetley[1], Henry De Belly[1,3], Spyridon Makris[1], Agnesska C. Benjamin[1], Ewa K. Paluch[1,3], Yanlan Mao[1,2], and Sophie E. Acton[1,✉]

[1]MRC Laboratory for Molecular Cell Biology and Department of Cell and Developmental Biology, University College London, Gower Street, London, WC1E 6BT, UK
[2]Institute for the Physics of Living Systems, University College London, Gower Street, London WC1E 6BT, UK
[3]Physiological Laboratory, Department of Physiology, Development and Neuroscience, University of Cambridge, CB2 3EG, UK

After immunogenic challenge, the lymph node rapidly increases in cellularity making space for infiltrating and dividing lymphocytes, expanding the tissue. In the early phases of expansion, the underlying fibroblastic stroma, which organises the lymph node, undergoes elongation and stretching. This is followed by the initiation of fibroblastic stroma proliferation as inflammation proceeds. In the steady state, fibroblastic reticular cells (FRCs) tightly wrap an interconnected network of extracellular matrix fibres. The initial physical deformability of the lymph node is in part determined by Podoplanin (PDPN) signalling in FRCs and is modulated by dendritic cells expressing c-type lectin receptor 2 (CLEC-2). However, the mechanisms changing tissue and cellular mechanical forces of the fibroblastic stroma and the triggers for FRC proliferation and growth are unknown. We examined the contributions of FRC actomyosin contractility and extracellular matrix to lymph node tissue tension. Further, we directly tested the impact of tissue mechanics on the kinetics of lymph node expansion. We show using laser ablation that the FRC network is under mechanical tension generated by actomyosin contractility and that tension changes throughout the course of immunogenic challenge. We find that CLEC-2/PDPN signalling alters the cell intrinsic mechanical state of FRCs by reducing cortical tension and increasing FRC size. We found that FRC network tension is a critical cue in controlling lymph node expansion gating the initiation of FRC proliferation. Together this study demonstrates mechanical forces are generated and sensed through the FRC network to determine lymph node expansion required for an adaptive immune response.

Lymph node | Fibroblastic reticular cell | Podoplanin | Network tension | Tissue remodelling

Correspondence: ***s.acton@ucl.ac.uk***

Introduction

Upon immunogenic challenge, the lymph node (LN) rapidly remodels to accommodate increased lymph flow, trapping of naïve lymphocytes, and proliferation of activated T and B cell populations (1). How the underlying stromal architecture remodels during rapid tissue expansion, whilst supporting T and B cell compartmentalisation, is not understood. Four common stromal subsets are defined within LNs: fibroblastic reticular cells (PDPN$^+$CD31$^-$), blood endothelial cells (PDPN$^-$CD31$^+$), lymphatic endothelial cells (PDPN$^+$CD31$^+$) and double negative cells (PDPN$^-$CD31$^-$) (2). LN fibroblastic reticular cells (FRCs) provide a physical scaffold that defines the boundary and size of the tissue (3, 4). It is now well established that fibroblastic stroma are not inert scaffolds but indeed central players in adaptive immunity, supporting immunologically active niches within the tissue (4).

FRCs are the most populous stromal subset generating a reticular network and are associated with bundled extracellular matrix (ECM) fibres spanning the T-cell area and interfollicular regions of the tissue (2, 5). Recent single cell sequencing demonstrated the existence of different FRC subpopulations dependent on location and niche functions (6), however, FRCs form a continuous interconnected network spanning the whole tissue. FRCs broadly support lymphocyte homeostasis and maintenance of peripheral tolerance in the steady state (4, 7), and provide trafficking routes to facilitate the interactions between antigen-presenting dendritic cells and their cognate T cells (8). Remarkably, during LN expansion, FRC network connectivity is maintained suggesting that network connectivity is prioritised and is critical for the function of the tissue (9, 10). Initially, FRCs elongate and increase in cell volume before entering a period of proliferation as inflammation proceeds. However, it is not currently known, at the tissue or cellular level, what forces are generated as the LN rapidly expands and how FRCs respond to these forces.

As the LN expands, mechanical forces may arise from external tissue scale properties such as cellular compression, fluid flow, ECM remodelling or mechanical stretch (11, 12). Tissues and cells have a range of mechanisms to dissipate or resist mechanical stresses to prevent tissue damage, such as elasticity & material stiffness (13), shape change, actomyosin contractility, regulation of adhesion, or opening of stretch sensitive channels (12, 14). A constant balance of cell derived and external mechanical forces to preserve tissue integrity is achieved through coupling forces to biochemical signalling pathways (15). It has been shown that LNs get softer or more deformable as they initially expand (16, 17) but it is not known how the contractile forces exerted by FRCs, measured *in vitro* (5, 17), convert to mechanical force generation by the FRC network inside the LN tissue. FRCs elongate in the early phase of the immune response, and these cell shape changes will require altered cell surface mechanics and actomyosin contractility (18, 19). However, actomyosin

regulation in FRCs has only been studied directly *in vitro*. Previous studies have asserted that myofibroblastic features of FRCs generate contractile forces to set tissue size. This has been demonstrated through *in vitro* wrinkle & contraction assays (16, 17) and expression of the prototypical markers of myofibroblasts such as alpha smooth muscle actin (α-SMA) (2, 20). However, α-SMA has primarily been used to determine the development state of FRCs (20) and α-SMA tissue staining has yielded varying results with some studies showing very low α-SMA in the steady state LN (1, 5). In steady state FRCs, PDPN connects the actin cytoskeleton to the cell membrane through ERM (Ezrin-radixin-Moesin) and generates actomyosin contractility through activation of RhoA/C and its effector Rho-kinase (ROCK), which controls phosphorylation of myosin light chain (MLC) (21). *In vivo* studies have shown that CLEC-2$^+$ DCs binding to PDPN$^+$ FRCs (CLEC-2/PDPN signalling axis) downregulates FRC actomyosin contractility, permitting stretching and spreading of the FRC network (16, 17). This allows FRCs to change shape and increase cell volume to span over a larger tissue area as the LN expands (16, 17). However, CLEC-2/PDPN signalling peaks in the first 72 hours of an adaptive immune response, as CLEC-2$^+$ DCs migrate into the LN from the peripheral tissue. CLEC-2 mediated inhibition of actomyosin contractility permits the FRC network to expand before proliferation of FRCs is observed. The exact timing of when FRCs transition from stretching to proliferation varies between experimental models of the kinetics of LN expansion. Many chemical signals have been suggested to induce FRC proliferation, including cytokines such as lymphotoxin (LT), IL-17 (22), CLEC-2 binding (16) and T-cell trapping (1).

In this study we investigated the role of mechanical forces in guiding LN expansion and maintaining FRC network connectivity. We hypothesized that the FRC network generates and responds to mechanical forces during expansion. We further hypothesized that changes in the mechanical tension of the FRC network may better explain the synchronous induction of FRC proliferation later in the immune response. Using a combination of *ex vivo* and *in vitro* biophysical assays we showed that actomyosin structures present within the FRC network *in vivo* generate mechanical tension that changes throughout immunogenic challenge. We implicate the CLEC-2/PDPN signalling pathway in regulating cell surface mechanics of FRCs. Finally, we found that FRC network tension is a critical cue in controlling LN expansion gating the initiation of FRC proliferation.

Results

Filamentous actin structures persist in the FRC network through LN expansion. It is known that the CLEC-2/PDPN signalling axis reduces actomyosin contractility in FRCs *in vitro*, and that this signal is required for acute LN expansion (16, 17). However, contractile actin structures in FRCs have not previously been visualised in LN tissue, in steady state or during LN expansion. Furthermore, previous studies do not address the contribution of the extracellular matrix to the contractile state of the FRC network. We used confocal microscopy of LN tissues to map the sub-cellular location of actomyosin structures in FRCs and their relationship with the underlying extracellular matrix structures of the conduit. The FRC network, identified by PDPN expression (yellow), spans the whole LN tissue but specifically supports T cell function (CD3$^+$ blue) in the paracortex, providing trafficking routes (8, 23) from high endothelial venules (24) to B cell follicles (25) (Figure 1A). At the tissue scale, staining of perlecan, which marks the basement membrane on the outer layer of the ECM conduit (26), and PDPN showed that F-actin structures are enriched in the steady state FRC network, subcapsular sinus, HEV and the medullary regions (Supplementary figure 1A, Supplementary movie 1A-C). To examine the F-actin structures in the FRC network in response to immunogenic challenge we immunised mice with incomplete Freund's adjuvant and ovalbumin (IFA/OVA) to drive LN expansion (Supplementary figure 1A). The overall steady state pattern and intensity of F-actin staining was unchanged at days 3 and 5 post immunisation (Supplementary figure 1A, Supplementary movie 1A-C). F-actin intensity through the T cell FRC network was quantified by using PDPN staining as a mask (Figure 1B). Whilst PDPN intensity increased (Figure 1C) as inflammation proceeded, as has been noted in other studies (10, 27), F-actin cables were maintained in the network through to day 5 post immunisation (Figure 1D).

At the cellular scale, we observe F-actin structures contained inside the PDPN$^+$ FRC body (Figure 1E, Supplementary Movie 2A). Maximum projections and orthogonal views of the FRCs show F-actin structures aligned both proximal to the basement membrane (white asterix) and spanning beneath the T-cell-facing FRC plasma membrane (white arrowheads) (Figure 1E, Supplementary Movie 2A-C). Immunofluorescence staining for the phosphorylation of myosin regulatory light chain (pMLC2 (S19)), colocalised with F-actin filaments, indicating that they are contractile (Figure 1E). In reactive LNs, 3 days after IFA/OVA immunisation, F-actin structures were still clearly visible throughout the FRC network (Figure 1E, Supplementary Movie 2B). However, the F-actin structures were located primarily proximal to the basement membrane (white asterix), and fewer T-cell facing actin cables were observed compared to steady state. pMLC staining was not always colocalised with F-actin (Figure 1E orthogonal view). 5 days post immunisation the LN is approximately 3-5 times larger. During this phase of expansion, the conduit network becomes partially fragmented, as has been previously reported (10), yet FRCs were connected with their neighbours even in the absence of extracellular matrix scaffolds (Figure 1E). Interestingly, prominent F-actin structures are still clearly observed spanning FRCs which are no longer associated with the ECM conduit (white arrowhead). Where conduit matrix structures persisted, F-actin cables were proximal to conduits (white asterix) (Figure 1E).

Together, the presence of the actomyosin structures suggest the FRCs are generating reactive and productive forces (28) to resist changing forces in the external environment as the LN expands. Further, attachment to the extracellular matrix is not required for the formation of actomyosin cables (Fig-

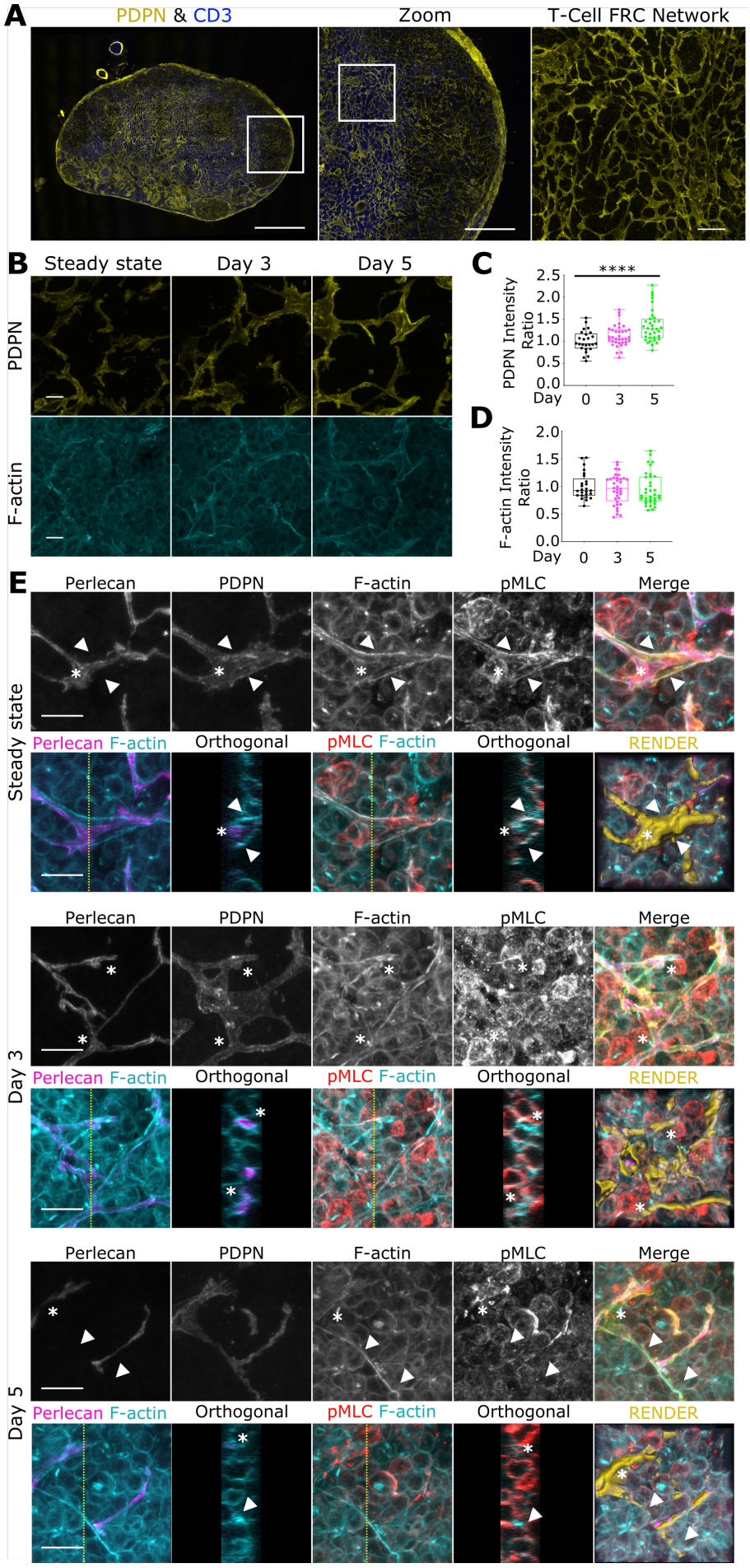

Fig. 1. Filamentous actin structures persist in the FRC network throughout LN expansion A) Tile scan (left) maximum Z projection (19µm) of inguinal LN stained for PDPN and CD3, scale bar 500µm. Digital zoom (middle) demonstrates the T cell and B cell border region marked by CD3 positive staining, scale bar 200µm. The T-cell area (right) representing the prototypical FRC reticular network stained with PDPN. Scale bar 25µm. B) Representative max projections (30µm) of F-actin (cyan) and PDPN (yellow) for quantification across immunisation. Scale bar 10µm. C) Quantification of the mean gray value of PDPN staining across the whole image ROI throughout inflammation compared to steady state. Box plots indicates median and interquartile range. One-way ANOVA with Tukeys multiple comparisons, $p<0.0001$. N>5 animals per condition. D) Quantification of the mean gray value of PDPN+ F-actin staining region compared to F-actin in the whole image ROI throughout inflammation compared to steady state. Box plots indicates median and interquartile range. One-way ANOVA with Tukeys multiple comparisons. N>5 animals per condition. E) Representative zooms of the T cell area FRCs throughout inflammation. Individual grey scale images of perlecan (conduit), PDPN (FRC network), phalloidin (F-actin) and pMLC. Examples of F-actin cables in relation to the perlecan conduit shows T-cell facing (white arrowheads) or aligned to the conduit (white asterisk). Orthogonal views (yellow dotted line, YZ axis, 10µm depth) show F-actin and perlecan in cross section. pMLC and F-actin overlap is denoted by white colocalization. The actomyosin structures are contained within the PDPN render (yellow). Scale bar 10µm.

ure 1E). The T-cell-facing F-actin filaments are reminiscent of actomyosin dependent, cell edge F-actin cables, observed *in vitro*, generated in response to inward membrane tension in the absence of underlying adhesive substrates (29, 30). The actomyosin cables we observe in FRCs would imply that the FRCs are resisting and balancing forces both in the steady state and as the tissue expands. However, our static observations cannot directly quantify forces within the FRC network.

Active actomyosin structures generate mechanical tension in the FRC network in situ. After identifying actomyosin structures within the FRC network (Figure 1E) we asked whether this leads to mechanical tension in the FRC network. We directly measured the recoil of the FRC network following laser ablation (31) in LNs expressing fibroblast-specific membrane GFP (Figure 2A, Supplementary Figure 2A, 3A). Culture of live *ex vivo* LN tissue slices (200µm) permitted mechanical measurements whilst retaining the tissue architecture, specifically T-cell compaction and FRC network integrity (Figure 2B, Supplementary Figure 3A). We could then compare mechanical tension in the steady state and during the early phase of LN expansion (Figure 2C), before FRCs are induced to proliferate (1, 16, 17). In the steady state, single ablation cuts of the network resulted in immediate recoil of the network in both directions away from the cut site (Figure 2D, Supplementary Movie 3A). Mean initial recoil velocity of 0.42µm/s^{-1} demonstrated mechanical tension within the network in the steady state (Figure 2E-F). This demonstrates that the FRC network is indeed contractile in agreement with previous studies (1, 2, 5, 16, 17), generating tension in the tissue. Moreover, tension was heterogenous (SD between 0.12 and 0.33) suggesting forces are not uniformly distributed through the tissue (Supplementary figure 3B-D), consistent with observations in other tissues and model systems (32, 33).

We hypothesised that increased T-cells numbers (1) would exert greater forces on the FRC network and therefore require increased resistive force, thus increasing tension, to prevent rupture of the network. Surprisingly, at day 3 post immunisation recoil was decreased by 29% to 0.30µm/s^{-1} (Figure 2D-F, Supplementary Movie 3B) despite a 1.5-fold increase in tissue mass (Figure 2C). However, after the LN had continued to expand at day 5 post immunisation (Figure 2C), the mean initial recoil velocity was 60% higher than in the steady state at 0.71µm/s^{-1} (Figure 2D-F, Supplementary Movie 3C). We also observed that at day 3 network recoil was contained in the region closest to the ablation site, whereas recoil propagated across the whole imaging ROI in both steady state and Day 5 conditions (Figure 2D, white arrowheads).

Actomyosin contractility of FRCs determine LN expansion (16, 17). To test the contribution of actomyosin contractility to tissue tension (Figure 1) we inhibited contractility with Y-27632 (Y27), an inhibitor of Rho associated kinase (ROCK), a key activator of myosin II (34). Treatment of steady state LN slices with ROCK inhibitor led to a 50% reduction in initial recoil velocities to 0.36µm/s^{-1}, whilst maintaining the architecture of the FRC network (Figure 2G, Supplementary figure 3E-F). However, inhibition of ROCK showed no significant effect in reducing tension at day 3 (Figure 2G). The most striking effect of ROCK inhibition was observed in day 5 draining LN slices whereby the 2-fold increase in recoil compared to the steady state was completely abolished to 0.30µm/s^{-1} (Figure 2G, Supplementary figure 3B-E). These data show that FRC network tension is actomyosin-dependent and varies in response to LN expansion. Further, it appears that ECM does not significantly contribute to the increased network tension observed at day 5, since at this timepoint the conduit structure is partially disrupted (Figure 1E) as has been previously shown (10). We conclude that FRC network tension changes through immunogenic challenge and is driven by cell intrinsic factors. Since it is known that the CLEC-2/PDPN signalling axis is a key driver of actomyosin contractility in FRCs, we investigated how this pathway contributes to the cell-intrinsic mechanical state of FRCs.

Membrane tension of FRC's is decreased through the CLEC-2/PDPN signalling axis. In order to permit shape change and spreading across larger distances, the cell surface mechanics of the FRC must change. Apparent membrane tension (hereafter membrane tension), a feature of cell surface mechanics, regulates spreading, cell shape change and cell fate (35–37). Membrane tension is determined by the in-plane tension of the lipid bilayer and the strength of membrane-to-cortex attachments (37, 38). Membrane tension can be quantified by measuring the resistance of the plasma membrane to deformation (36, 39). PDPN is known to directly interact with ezrin, a member of the ERM, (Ezrin, Raxidin, Moesin) protein family, which physically links the actin cortex to the membrane (40–42). Furthermore, a tetraspanin binding partner of PDPN, CD44, is also known to bind to ERM proteins (21, 27). CLEC-2 binding decouples ezrin from PDPN, and displaces ezrin from the membrane (16) but how CLEC-2 binding impacts cell surface mechanics has not been measured. We tested whether CLEC-2/PDPN signalling impacts membrane tension of FRCs.

We used a tether pulling assay using optical tweezers in which force exerted on a bead by a plasma membrane tether, the trap force (F_t), is a direct readout of membrane tension (Figure 3A, Supplementary Movie 4) (36, 37). We measured a steady state membrane tension of 56.2pN in FRCs (Figure 3B) similar to the membrane tension reported for other adherent cell lines (36, 37, 43). Pre-treatment of FRCs with recombinant CLEC-2 is sufficient to decrease membrane tension by approximately 40% to 39.2pN (Figure 3B). We could observe an equivalent decrease in the membrane tension in individual FRCs taking measurements before and after just 15 minutes of CLEC-2 treatment (Figure 3C). Furthermore, PDPN knockdown (PDPN KD) cell lines also had lower membrane tension than control cells (29.7pN), demonstrating the importance of PDPN in maintaining steady state membrane tension. It is important to confirm that CLEC-2 acts specifically through PDPN. CLEC-2 treatment of PDPN KO FRCs has no affect on membrane tension (Supplementary Figure 4B), validating CLEC-2 reduces membrane tension through PDPN engagement. To ask if PDPN is the predominant

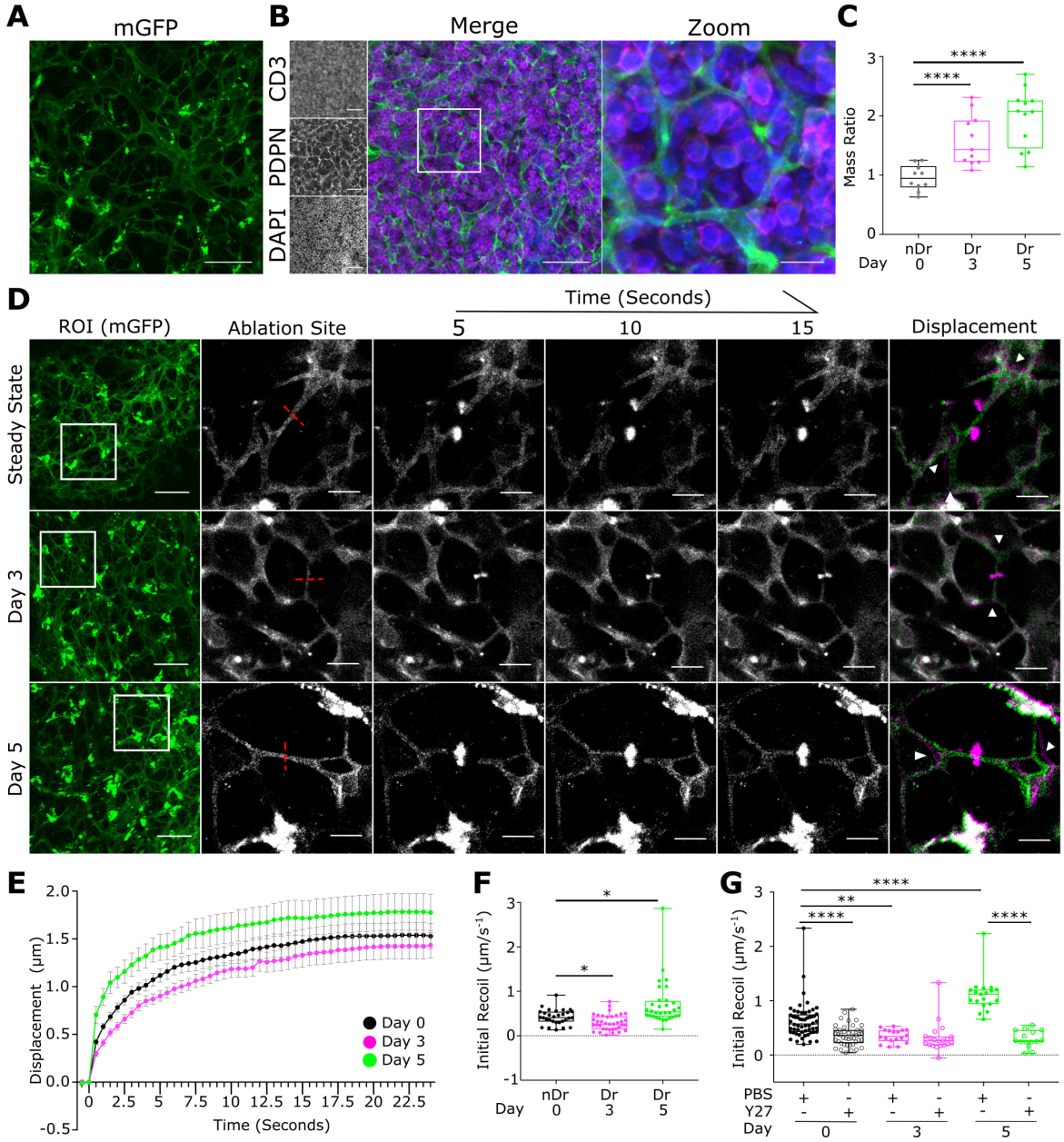

Fig. 2. Active actomyosin structures generate mechanical tension in the FRC network in situ A) Membrane GFP visualises the FRC network in the *ex vivo* lymph node slice. Scale bar 50µm. B) *Ex vivo* cultures maintain FRC network structure and T-cell compaction. PDPN (FRC network, green), CD3 (T cells, purple), DAPI (Nuclei, blue). Scale bar 50µm. White box indicates zoomed region. Scale bar 10µm. C) Mass increase relative to non-immunised (Day 0). N>5 animals per condition. D) Region of interest (ROI) shows structure of the FRC network and a representative image of a zoom used during and ablation experiment region of ablation (white square). Scale bar 50µm. Red dotted line indicates ablation cut. Recoil visualised (white arrowheads, right) with pre (green) and 15 sec post cut (magenta) overlay. White colocalization indicate areas where there is no recoil over the imaging time. Scale bar 10µm. E) Recoil curves show displacement over time (mean ±SEM). N>5 animals per condition. F) Initial recoil velocity (µm/s^{-1}) measured by the displacement of the network immediately after ablation. Box plots indicates median and interquartile range. ANOVA with Kruskal's multiple comparisons, $p<0.05$. N>5 animals per condition. G) Initial recoil velocity (µm/s^{-1}) measured after pre-treatment of slices with ROCK inhibitor Y27632. Box plots indicates median and interquartile range. Two-way ANOVA with Tukeys multiple comparisons, **$p<0.01$, ****$p<0.0001$. N>5 animals per condition

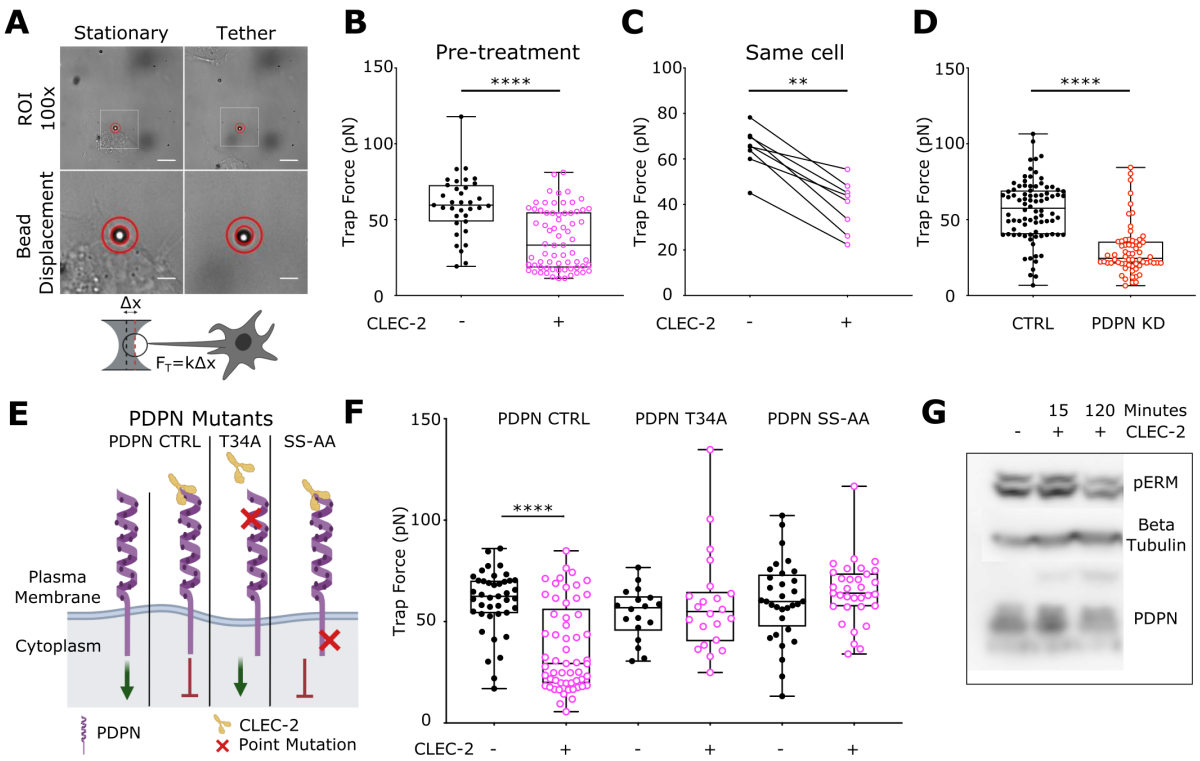

Fig. 3. Membrane tension of fibroblastic reticular cells is decreased through the CLEC-2/PDPN signalling axis A) Representative images of optical tweezers generating membrane tethers of FRCs (top panel). Scale bar 10µm. White box indicates zooms between stationery (bottom left) and tether (bottom right) showing bead displacement (red circles). Scale bar 2µm. Schema and equation to calculate trap force (F_t) from displacement (bottom). B) FRCs pre-treated with CLEC-2 prior to measurement of Trap force (pN). Box plots indicates median and interquartile range. Mann-Whitney test, p<0.001. Each point represents one cell. N>35. C) Trap force measurements of the same cell before and after CLEC-2 treatment. Wilcoxon test, p<0.01. Each point represents paired cell. N = 8. D) Trap force measurement of PDPN shRNA KD FRCs. Box plots indicates median and interquartile range. Mann-Whitney test, p<0.001. Each point represents one cell. N>64. E) Schema of exogenous PDPN mutants and interaction with CLEC-2. Green arrow denotes active signalling by PDPN leading to actomyosin contractility, red arrow indicates inhibition of PDPN signalling and reduction in actomyosin contractility. F) Trap force measurements of FRCs expressing PDPN mutants after pre-treatment of CLEC-2. Box plots indicates median and interquartile range. Two-way ANOVA with Tukeys multiple comparisons, p<0.001. N>18. G) Representative western blot of pERM in CTRL FRCs after treatment with CLEC-2.

determinant of steady state membrane tension we knocked out CD44, which can also directly interact with ERM, in FRCs expressing endogenous PDPN. However, we found that CD44 KO did not affect steady state membrane tension (Supplementary Figure 4C). We utilised PDPN knockout (PDPN KO) FRCs expressing exogenous PDPN mutants which affect their function (Figure 3E, Supplementary Figure 4A). When wild-type (WT) PDPN was exogenously expressed treatment with CLEC-2 was able to mimic the reduction of membrane tension (Figure 3F) similarly to control FRCs expressing endogenous PDPN. However, CLEC-2 had no affect on membrane tension in FRCs expressing PDPN T34A, a key residue required CLEC-2 binding (Figure 3E, F) 45. Further, CLEC-2 had no affect on membrane tension in FRCs expressing PDPN S167A S171A, two point mutations of the intracellular tail, required for downstream signalling (Figure 3E, F) (44, 45). Finally, we checked the phosphorylation status of ERM proteins following CLEC-2 treatment by western blot, and in agreement with our direct measurements of membrane tension, pERM levels are robustly reduced (Figure 3G). Together these data demonstrate the specificity of CLEC-2 binding to PDPN and the requirement for the PDPN cytoplasmic tail and downstream regulation of ERM to control FRC membrane tension.

Membrane availability in FRC's is increased through the CLEC-2/PDPN signalling axis. As the LN and the FRC network expand it has been observed that FRCs increase in cell volume before they proliferate (16). Since the CLEC-2/PDPN axis downregulates FRC membrane tension by decreasing ERM phosphorylation we asked whether the resulting reduction in actin cortex to membrane attachment facilitates the use of membrane reservoirs in FRCs allowing them to increase in volume (46, 47). To test this hypothesis, we used an osmotic shock assay (48) where the ionic conditions are maintained but the osmolarity is altered to force water into a cell. This causes rapid cell swelling, forcing the cell to increase their surface area and volume (Figure 4A, B) (48–50). We found that under hypotonic conditions PDPN WT FRCs were able to swell to approximately 1.2 times in diameter within 15 minutes (Figure 4C, Supplementary Movie 5A). Pre-treatment of control FRCs with CLEC-2 significantly increased the swelling capacity of the FRCs (Figure 4C, black dashed line). However, FRCs expressing PDPN T34A (which is unable to bind CLEC-2) did not show increase in swelling following CLEC-2 pre-treatment (Figure 4D, Supplementary Movie 5B), confirming that the increased swelling capacity observed in control FRCs was specific to the CLEC-2/PDPN signalling axis.

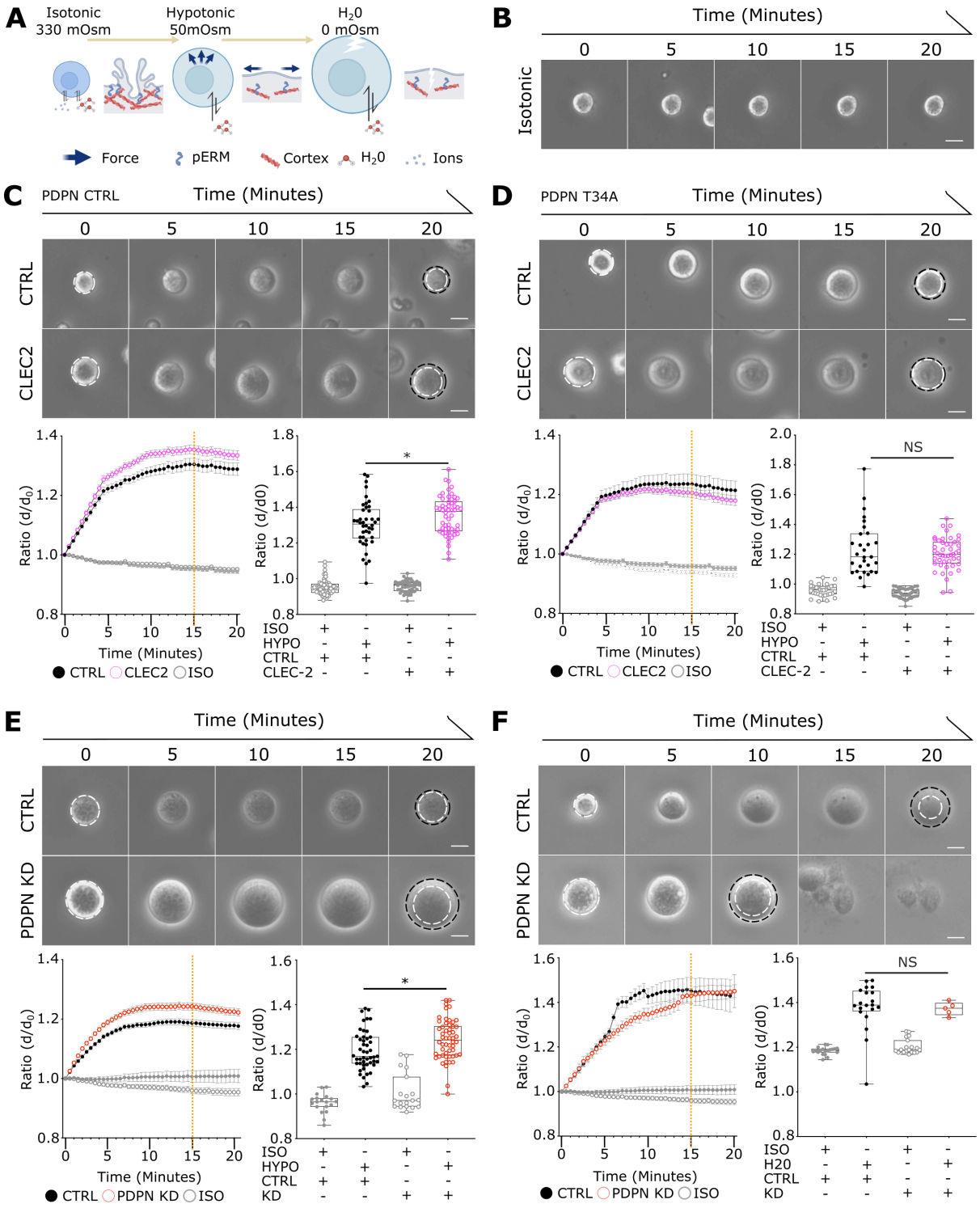

Fig. 4. Membrane access of fibroblastic reticular cells is increased through the CLEC-2/PDPN signalling axis A) Schematic of osmotic shock experiment, inducing swelling by altering osmolarity. B) Representative stills of FRC in isotonic control media. Scale bar 25µm. C) Time course of PDPN CTRL FRCs with or without CLEC-2 treatment in hypotonic conditions. Stills (top) show swelling of cells in hypotonic media. White dotted circle marks initial size before swelling and is compared to swelling at t=20 (black dotted circle). Scale bar 25µm. Change in diameter ratio over time (bottom left, mean ±SEM). Swelling ratio comparisons between control and CLEC-2 treatment at 15 minutes post swelling (orange dotted line, bottom right). Box plots indicates median and interquartile range. One-way ANOVA with Tukeys multiple comparisons, $p<0.01$. N>42. D) Time course of PDPN T34A FRCs with or without CLEC-2 treatment in hypotonic conditions. Stills (top) show swelling of cells in hypotonic media. White dotted circle marks initial size before swelling and is compared to swelling at t=20 (black dotted circle). Scale bar 25µm. Change in diameter ratio over time (bottom left, mean ±SEM). Swelling ratio comparisons between control and CLEC-2 treatment at 15 minutes post swelling (orange dotted line, bottom right). Box plots indicates median and interquartile range. One-way ANOVA with Tukeys multiple comparisons. N>29. E) Time course of PDPN CTRL vs PDPN shRNA KD FRCs in hypotonic conditions. Stills (top) show swelling of cells in hypotonic media. White dotted circle marks initial size before swelling and is compared to swelling at t=20 (black dotted circle). Scale bar 25µm. Change in diameter ratio over time (bottom left, mean ±SEM). Swelling ratio comparisons between control and PDPN shRNA KD FRCs at 15 minutes post swelling (orange dotted line, bottom right). Box plots indicates median and interquartile range. One-way ANOVA with Tukeys multiple comparisons, $p<0.0001$. N>19. F) Time course of PDPN CTRL vs PDPN shRNA KD FRCs in extreme hypotonic conditions (H20). Stills (top) show swelling of cells in hypotonic media. White dotted circle marks initial size before swelling and is compared to swelling at t=20 (black dotted circle). Scale bar 25µm. Change in diameter ratio over time (bottom left, mean ±SEM). Swelling ratio between control and PDPN shRNA KD FRCs at 15 minutes post swelling (orange dotted line, bottom right). Box plots indicates median and interquartile range. One-way ANOVA with Tukeys multiple comparisons. N>16.

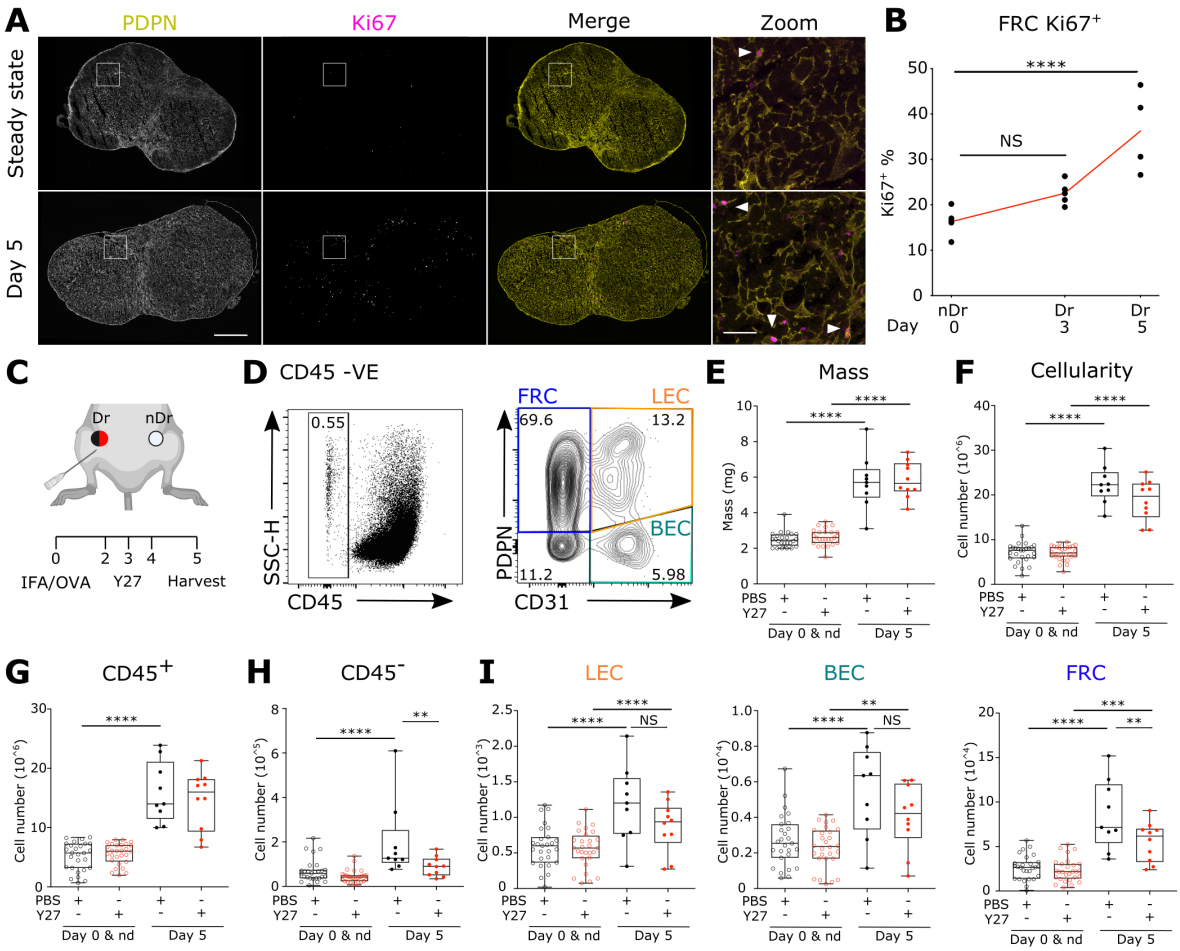

Fig. 5. Mechanical tension is required for complete FRC remodelling during inflammation A) Representative tile scan of PDPN$^+$ (left) and Ki67$^+$ (middle) and merged staining across an inguinal LN section (right). Scale bar 500µm. White box indicates region of digital zoom in T-cell area (zoom). Scale bar 50µm. White arrowheads mark PDPN$^+$ Ki67$^+$ FRCs. B) Flow cytometric analysis of Ki67$^+$ percentage of FRC's during acute inflammation. Red line represents the mean. Two-way ANOVA with Tukeys multiple comparisons, p<0.0001. N>4 animals per condition. C) Schematic of immunisation and Y27 treatment timeline. D) Representative flow cytometric gating of stromal cells (left) and stromal specific populations (right). Values represent percentage of parent population. E) Lymph node mass. Box plots indicates median and interquartile range. Two-way ANOVA with Tukeys multiple comparisons, ****p<0.0001, ***p<0.001. N>9 animals per condition. F-G) Total number of cells, CD45$^-$, CD45$^+$. I) Total number of LECs (left), BECs (middle) and FRCs (right). Box plots indicates median and interquartile range. Two-way ANOVA with Tukeys multiple comparisons, ****p<0.0001, ***p<0.001, **p<0.01. N>9 animals per condition

The hypotonic conditions require cells to increase their surface area, and therefore their plasma membrane. This can be achieved either by more rapid access to the cell's existing membrane reservoirs, such as active caveolae (Supplementary Figure 5A), or increased membrane production. To test whether PDPN regulates membrane production we compared the swelling capacity of control (CTRL) and PDPN KD FRCs. PDPN KD cells could swell more than CTRL cells in hypotonic conditions (Figure 4E, Supplementary Movie 5C), phenocopying the effects of CLEC-2 treatment (Figure 4C). However, when we applied extreme hypotonicity conditions both control and PDPN KD cell lines swelled to the same maximal ratio (Figure 4F, Supplementary Movie 5D). We therefore suggest that PDPN does not increase the total amount of membrane but instead regulates membrane-cortex attachment, and therefore access to existing membrane reservoirs (Supplementary Figure 5A) as cells increase in volume. Together these data suggest that the CLEC-2/PDPN axis permits increased FRC network deformability by regulating the cell surface mechanics of FRCs. It is known that CLEC-2 expression is specifically required on DC's (CD11c$^+$) for LN expansion, which increase in numbers in the LN during the first 1-4 days of the immune response (16, 51), suggesting that the mechanical softening of FRCs is an early, transient phase of LN tissue remodelling. This is consistent with the reduced tissue tension we measure 3 days post immunisation (Figure 2E-G), and gives us mechanistic insight into how the FRCs network is able to elongate and stretch in the early phases of LN expansion.

Mechanical tension is required for induction of FRC proliferation *in vivo*. During an adaptive immune response, lymphocyte trapping and proliferation drive expansion of the LN. Several studies of LN expansion have found that the FRC population lags behind in cell number, and proliferate later (3-5 days) in the immune response (1, 16, 17, 52). It is not known how FRC proliferation is triggered. We hypothesised that increased mechanical tension at day 5 (Figure 2) may act

as a cue to initiate FRC cell division. We examined FRC proliferation in reactive LN's by immunofluorescence. It is not known whether all FRCs throughout the tissue respond synchronously or whether specific FRC subpopulations are preferentially proliferative to grow the FRC network as the LN expands (4). To determine the proliferative state of the LN we quantified cell cycle entry by staining for Ki67$^+$ cells. Day 5 LN's showed a clear increase in Ki67$^+$ staining compared to steady state, with staining distributed throughout the whole tissue (Figure 5A). Using PDPN staining as a mask, we could quantify Ki67$^+$ FRCs (Figure 5A white arrowheads). As expected at day 5 the majority of Ki67$^+$ cells in the tissue are lymphocytes (Supplementary Figure 6A (left)), however we could also confirm that a higher number of FRCs had entered the cell cycle (Supplementary Figure 6A (right)). We validated these observations using flow cytometry and found that in steady state less than 20% of FRCs were Ki67$^+$ (Figure 5B), indicating that the majority of FRCs exist in G_0 in steady state and are not actively in the cell cycle (4). The low proportion of Ki67$^+$ FRCs is maintained 3 days post immunisation indicating that FRCs are still not proliferating at this point (Figure 5B). However, the percentage of Ki67$^+$ FRCs doubles between day 3 and day 5 post immunisation (Figure 5B), highlighting the beginning of the FRC proliferative phase for LN expansion. Other studies have estimated that up to 60% of FRCs are actively proliferating 2 weeks following immunisation (1, 52). The timing of the increase in PDPN$^+$ Ki67$^+$ cells correlated with the increase in mechanical tension within the FRC network (Figure 5A-B, Figure 2E-G). This correlation raised the hypothesis that increased mechanical tension in the FRC network may gate the induction of FRC proliferation.

The FRC network tension in steady state and the increased tension measured at day 5 were both abolished by the inhibition of actomyosin contractility (Figure 2G). Therefore, we examined LN stromal populations through early LN expansion following inhibition of ROCK *in vivo* (Figure 5C-D) (34, 53). Inhibition of ROCK had no effect on LN mass or cellularity (Figure 5E,F) indicating that LNs can still expand similarly to controls, and importantly, expansion of CD45$^+$ immune cell populations was unaffected (Figure 5G).

However, the CD45$^-$ stromal cell population was reduced approximately 50% compared to controls 5 days post immunisation (Figure 5H). We found that FRCs were specifically reduced in cell number following inhibition of actomyosin contractility (Figure 5I), accounting for the majority of the reduction in the stromal cell population. Endothelial populations of BECs and LECs, although not significantly reduced in number by the decrease of actomyosin activity, also showed a downward trend (Figure 5I). Together these data demonstrate that LN's require actomyosin contractility to increase stromal cell number required for tissue expansion. FRCs were the most sensitive stromal subtype (Figure 5I), with reduction of contractility in the FRC network delaying the kinetics of FRC proliferation (Supplementary Figure 6D), demonstrating that the FRC network responds to mechanical strain during LN expansion.

Discussion

LN expansion and resolution is a cyclic and controlled processes requiring extensive remodelling of the underlying stroma which set up and maintain tissue architecture. The size of the LN is a readout of the balance between expansive forces, driven by increased T-cell trapping and proliferation, and contractile forces of the FRC network (1, 4, 16). Here we show that in the steady state tissue, mechanical tension in the FRC network is generated through active actomyosin contractility (Figure 2F-G). Furthermore, we observed a variety of actomyosin structures not previously investigated in the steady state LN, including T-cell plasma membrane facing F-actin cables which are reminiscent of cables formed at membranes resisting inward deformation (Figure 1E) (29, 30). Together, we suggest that this indicates that in the steady state FRCs are both generating mechanical tension to control tissue size but are also resisting compression from the surrounding T-cells, as a result of T-cell crowding, to maintain a space for the FRC cell body and conduit network.

Despite previous reports indicating actomyosin would be reduced during the CLEC-2$^+$ DCs phase of inflammation (16, 17), we still observed actomyosin structures inside the FRC network at day 3 (Figure 1E). However, despite the persistence of actomyosin cables, FRC network tension was reduced 3 days following immunisation (Figure 2F-G). Furthermore, inhibition of ROCK-dependent actomyosin contractility did not induce any further decrease in tension at day 3 (Figure 2G).

These data provide mechanical measurements that support previous observations asserting CLEC-2/PDPN signalling leads to reduction in FRC contractility, priming the tissue for expansion. However, in this study we go beyond the actomyosin regulation to show that CLEC-2/PDPN also regulates the cell membrane mechanics of FRCs. CLEC-2 signalling through PDPN leads to dephosphorylation of ERM proteins resulting in a reduction in membrane cortical tension, a prerequisite for cell spreading and shape change. This signalling pathway would provide a mechanism by which FRCs can become both more deformable and spread over a larger area as the LN expands, whilst also producing resistive forces to preserve the network and the conduit in the earliest phase of the immune response.

The most striking mechanical feature that we observed is the actomyosin dependent and ECM independent increase in FRC network tension 5 days after immunisation (Figure 2F-G). This suggests the network is mechanically reactive to the increased tissue size driven by T-cell trapping and proliferation (1). This increase in tension coincides with the transition to increased FRC proliferation in the tissue. The mechanisms controlling initiation of FRC proliferation in the later phases of the immune response are still debated. Many chemical signals have been investigated, however, whether mechanical cues are a sufficient trigger for FRC proliferation had not been tested. We show here that inhibition of actomyosin contractility is sufficient to delay FRC proliferation, and moreover specifically impacts this key stromal cell subset. By maintaining the chemical cues that drive lymphocyte

expansion, whilst reducing FRC network tension, we showed that actomyosin contractility in the FRC network impacts the number of FRCs (Figure 5K).

There are several mechanisms through which FRCs may respond to increased mechanical tension, leading to an increase in proliferation, including cell-ECM integrin mechanosensing, cell-cell adhesion, translocation of YAP to the nucleus and opening of stretch-sensitive ion channels (54–56). Recently, it has been shown that in peyer's patches of the intestine, FRCs require the expression of the mechanosensor Piezo1 to detect fluid flow and mount a complete response to infection (57). However, deletion of piezo1 had no effect on LN remodelling (57). This may point to tissue-specific mechanical sensation in secondary lymphoid organs. YAP/TAZ signalling has been shown to regulate exit from pre-FRCs to immunologically competent FRCs in the adult tissue. However, deletion of YAP/TAZ in adult FRCs did not lead to any LN defects. In contrast, overactivation of YAP/TAZ through the deletion of LATS1/2 lead to myofibrosis in the tissue, therefore the role of YAP/TAZ in regulating FRCs in the adult tissue cannot be fully excluded (58). Indeed there is some evidence that YAP nuclear localisation maybe increased during LN expansion (17). The presence of F-actin structures in the absence of complete ECM at day 5 suggests that cell-cell adhesion may play a more important role in sensing mechanical forces, than cell-matrix adhesion. Single cell sequencing studies have revealed cadherin 11 as the most expressed junctional protein (2, 6). However, there is much still to discover about how FRCs connect to their neighbours in the tissue.

The understanding of mechanical forces and their regulation of FRC function in the LN is in its infancy. This study provides a framework of the changing mechanical tension during the early phase of an immune response. We hypothesise that the impact of mechanical tension is not limited to the initial phase of the immune response but may also contribute to setting the maximum tissue size and in returning the LN to its original state following an adaptive immune response. The impacts of the stromal mechanical environment of the LN on immune cell function should also be considered in future studies. It has been recently demonstrated that T-cell activation is modulated by the stiffness of mechanical environment, thus providing an additional layer of immune regulation that could be enacted by the FRC network (59, 60). Finally, it remains to be elucidated how the mechanical forces are sensed and coordinated across the tissue by FRCs. Our data further indicate that forces are buffered across the whole tissue to maintain FRC network and tissue integrity during an immune response, which raises a further question as to how forces and other signals can be coordinated throughout the stromal network.

ACKNOWLEDGEMENTS

We thank Dr Victor G. Martinez and Dr Charlotte M de Winde for critical reading of the manuscript. We thank Ki Hng, Andrew Vaughan, and the core staff at MRC-LMCB for light microscopy expertise and Dr Yanping Guo at the UCL Cancer institute flow cytometry facility for assistance in the work contained within the manuscript. This work was supported by the European Research Council Starting Grant (LNEXPANDS; to S.E.A), Cancer Research UK Careers Development Fellowship (CRUK-A19763; to S.E.A), Medical Research Council (MC-U12266B), MRC awards MR/L009056/1 and MR/T031646/1 (Y.M), Lister Institute Research Prize and EMBO Young Investigator Programme (Y.M), the European Union's Horizon 2020 research and innovation programme under the Marie Sklodowska-Curie grant agreement No 641639 (ITN Biopol, E.K.P) and the Medical Research Council UK (MRC programme award MC_UU_12018/5 (E.K.P).

Author contributions. H.L.H and S.E.A designed the study and wrote the manuscript. H.L.H performed and analysed all experiments. A.C.B. and S.E.A. generated the PDGFRα-mGFP-CreERT2 mouse model. R.J.T assisted with laser ablation studies. H.d.B assisted with optical trap measurements. H.d.B contribution was carried out under the support of E.K.P at MRC-LMCB UCL, current location is the department of Biochemistry and Biophysics, UCSF, San Francisco, CA, USA. S.M assisted with flow cytometry of stromal cells. Y.M and E.K.P contributed to study design and editing of the manuscript. All authors contributed to editing of the manuscript.

Materials and Methods

Mice. Experiments were performed in accordance with national and institutional guidelines for animal care and approved by the institutional animal ethics committee review board, European research council and the UK Home office. Breeding of animal lines were maintained off site at Charles River Laboratory. Wild type C57BL/6J mice were purchased from Charles River Laboratories. Novel mouse model of PDGFRα-mGFP-CreERT2 generation. EGFP with a membrane tag (N-terminal 0-20 amino acids of neuromodulin GAP-43) was inserted into the PDGFRα gene locus in combination with a CreERT2 cassette (linked to mGFP with a P2A self cleavage peptide cite (61)) using Cyagen CRISPR Cas9 technology. Females and males aged between 8-12 weeks were used for experiments, unless stated otherwise. Mice were immunised via subcutaneous injection into the right flank, proximal to the hip, with 100µl of an emulsion of Ovalbumin (OVA) with incomplete Freunds adjuvant (IFA) (100µg OVA per mouse) (Hooke Laboratories). Where stated, mice were treated with Y-27632 (Tocris 1254). 10µl of 1mg/ml Y-27632 dissolved in PBS was injected subcutaneously into the right flank, proximal to the hip. 10µl of sterile PBS was used as injection control. Y-27632/PBS injections were given on 3 consecutive days 24 hours post IFA/OVA injection. After 5 or 3 days mice were culled and inguinal LNs from both flanks (naïve and inflamed) were extracted for paired histological studies, flow cytometry analysis or *ex vivo* laser ablation.

***Ex vivo* LN cultures.** Preparation for *ex vivo* lymph nodes laser ablation was optimised following previously established methods (8, 62–64). UltraPureTM Low melting point agarose (Thermo Fischer Scientific) prepared in PBS at 3% w/v and maintained at 37°C. Lymph nodes were embedded into agarose and left for 5 minutes to set on ice. Lymph node blocks were secured by superglue to cutting stage and placed into ice cold PBS cutting chamber. Lecia Vibratome (VT1200S) 200µm thick sections were cut at a rate of 0.3mm/s and 1.5mm amplitude until the LN was completely sectioned. Collected sections were placed into RPMI 1640 containing 10% FBS, 1% penicillin and streptomycin (P/S) (Thermo Fischer scientific 15140122) and 1% Insulin-Transferrin-Selenium (ITS) (Thermo Fischer scientific 41400045) at 37°C, 10% CO_2. Sections recovered for an hour before been used for live imaging.

Laser ablation. LN sections were transferred to glass bottom 35mm MatTek dishes (P35G-1.5-20-C) with a small volume of RPMI media containing 1% P/S and 1% ITS. A glass cover slip was placed on top to secure the section. Sections imaged on a Zeiss LSM 880 inverted multiphoton microscope with the imaging chamber maintained at 37°C, 10% CO_2. Where stated, sections were treated with 100 µM Y-27632 (Tocris 1254) diluted in *ex vivo* culture media for at least 1 hour prior to imaging and ablation. Sections were imaged with a Plan Apochromat 40x oil objective (NA1.3), 1024*1024 resolution and 4x digital zoom for ablation ROIs. Laser ablation of the FRC network was achieved by using a pulsed Chameleon Vision II TiSa Laser power 75-80% (coherent) tuned to 760nm. Ablation was performed on small, manually defined linear regions of interest between FRC connections away from cell bodies. Ablation was performed in a single z-plane at the centre of the FRC connection in a vibratome slice. Time-lapse videos were recorded over 25 seconds on a single channel (PMT detector) 512*512 pixels, with 521 millisecond scan speed per frame to capture recoil of the network. Recoil of the network was calculated by manually measuring displacement of the FRC network between two points located away from the ablation site, with initial recoil velocities calculated from the displacement one frame after the cut, as in other studies (32, 65).

Immunostaining of LNs. LNs that were used for sectioning and immunofluorescence were fixed in Antigen fix (DiaPath) for 2 hours at 4°C with gentle agitation. LNs were washed for 30 minutes in PBS before being applied to 30% w/v sucrose 0.05% sodium azide solution at 4°C overnight. LNs were dipped into Tissue-Tek OCT before being embedded into moulds containing OCT. A maximum of six lymph nodes were embedded into a single block for comparative analysis. Lymph nodes were sectioned on the Leica cryostat at a thickness of 20um.

For immunofluorescent staining sections were permeabilised and blocked using 10% Normal goat serum (NGS), 0.3% Triton X-100 in PBS for two hours at room temperature. Primary antibodies were prepared by centrifugation at 13,000rpm for 5 minutes at 4°C. Primary antibodies were diluted according to Antibody Table 1 in 10% NGS, 0.01% Triton X-100 in PBS. Sections were incubated overnight at 4°C. Sections were then brought to room temperature and washed 3 times for 15 minutes each in 0.05% PBS-Tween20. Sections were then blocked using 10% Normal goat serum (NGS), 0.3% Triton X-100 in PBS for two hours at room temperature. Secondary antibodies were then prepared similarly to primary antibodies with dilutions in Antibody Table 1. Secondary antibodies were applied to sections for 2hrs at room temperature. This was followed by two 15 minute washes of 0.05% PBS-Tween20 and a final wash of 15 minutes in PBS. Sections were then mounted using mowiol mounting media.

For staining of 200µm thick vibratome sections, slices were first fixed in Antigen fix (DiaPath) for 2 hours at 4°C with gentle agitation. Sections were placed into 0.1M Tris-HCL pH7.4 on ice for 30 minutes. Sections were permeabilised using IHC buffer containing 0.5% BSA, 2% Triton X-100 (Sigma-Aldrich) in 0.1M Tris-HCL pH7.4 for 20 minutes at 4°C with gentle agitation. Primary antibodies were prepared by centrifugation at 13,000rpm for 5 minutes at 4°C. Primary antibodies were diluted into IHC buffer, according to Antibody Table 1, and applied to the sections for 1hr at 4°C with gentle agitation. Sections were then washed twice with 0.1M Tris-HCL for 15 minutes. Secondary antibodies were then prepared similarly to primary antibodies with dilutions in Antibody Table 1. Secondary antibodies were applied to sections for 1hr at 4°C with gentle agitation. Two final washes of 0.1M Tris-HCL were performed before mounting the sections with mowiol mounting media and a glass coverslip. Sections were then imaged on the Zeiss LSM 880 inverted multiphoton microscope using a Plan Apochromat 40x oil objective (NA1.3).

Unless otherwise stated confocal images were acquired using Leica TCS SP8 STED 3X or the Leica TCS SP5. Images were captured at 1024*1024 pixels, 3 line average onto HyD or PMT detectors. Fluorophore excitation and acquisition was performed in a sequential and bidirectional manner. Imaging regions were manually defined and z-stacks with regular z-intervals ranging from 0.4um or 1um (dependent on sample) were acquired using a motorised stage. Tile scans were automatically stitched (numerical) using Leica imaging software.

Flow cytometry of LNs. LNs were carefully dissected, weighed and placed into RPMI 1640 media on ice. LNs were then processed as previously described (16, 66). Briefly, LNs were placed into a digestion buffer containing collagenase D (250µg/ml) (Millipore Sigma), dispase II (800µg/ml) (Thermo Fisher Scientific) and DNase I (100µg/ml) (Sigma Aldrich). The lymph nodesLNs were genetly digested in a water bath at were incubated in a water bath at 37°C , removing and replacing the cell suspension every 10 minutes until completely digestedfor 20 minutes with gentle agitation. After the initial incubation lymph nodes were mixed every 10 minutes using a p1000 pipette to carefully digest the lymph node until the tissue was completely dissociated. Cell suspensions were then centrifuged at 350g for 5 minutes. The cells were resuspended into flow cytometry buffer (FACS) consisting of 1% BSA (Sigma Aldrich), 5mM EDTA (Sigma Aldrich) in PBS. The cell suspension was strained with a 70µm strainer (pluriSelect) and counted, filtered, counted and resuspended . The suspension was then centrifuged at 350g for 5 minutes and resuspended in 3ml of FACS buffer. For cell number counting, precision count bead^{TM} (Biolegend) were prepared at 1.03×10^6 particles/ml. After counting, cells were then centrifuged at 350g for 5 minutes before resuspending at the desired concentration of 10×10^6 cells/ml. 2.5×10^6 cells were then plated into 96 well plates for surface and intracellular staining of a stromal cell panel (Antibody Table 1). Cells were blocked with CD16/CD32 Mouse Fc block (BD) and then stained with primary antibodies for 20 minutes at 4°C. For intracellular staining of Ki67 cells were fixed and permeabilised using FOXP3 fix/perm buffer as specified inside the kit by the manufacturer (BioLegend).

Samples were run on the Fortessa X20 flow cytometer (BD Biosciences) at the UCL Cancer Institute. Data was analysed using Flow Jo software (FlowJo, LLC).

Cell lines. Immortalised fibroblastic reticular cells were generated as described in Acton et al 2014 (16, 27). Parental immortalised fibroblastic reticular cell line (Control FRC). PDPN was stably knocked down (PDPN KD FRC) in the parental cell line by transfection of a PDPN shRNA lentivirus. PDPN was completely depleted from the parental cell line (PDPN KO FRC) using CRISPR cas9 genetic deletion. In all experiment where PDPN mutant cell lines (PDPN WT, PDPN T34A, PDPN SS-AA) were used, protein production was induced by the addition of 1µg/ml of doxycycline for 48 hours. Cell lines were maintained at 10% CO_2, 37$^{\circ C}$ in Dulbecco's modified eagle medium (DMEM) (Thermo Fischer scientific) supplemented with 10% FBS, 1% P/S and 1% ITS unless otherwise stated. Cells were treated with recombinant CLEC2-Fc or Control-Fc supernatant (16, 27) for approximately 2 hours, where indicated, to assay the effect of CLEC2 signalling through PDPN. Figure 3C is a paired analysis of the same cell before and 15 minutes after CLEC-2 treatment.

Optical tweezer tether pulling. Trap force measurements were performed using a home built optical tweezer using a 4W 1064 nm laser quantum Ventus within a 100x oil immersion objective (NA 1.30, CFI Plan Fluor DLL, Nikon) on an inverted microscope (Nikon Eclipse TE2000-U) equipped with a motorised stage (PRIOR Proscan). The optical tweezer was calibrated following (36, 37). The trap force calibration was performed in every experiment with typical calibration trap stiffness of k=0.114 pN/nm. Measurements were performed using concanavalin-A coated (50ug/ml) carboxyl latex beads, (1.9um diameter, Thermo Fischer). Beads were incubated on a shaker with concanavalin-A for two hours prior to experiment. Beads were applied to the culture media, manipulated by the optical trap and brought into contact with the cellular membrane and typically held for 2-5 seconds to allow binding to membrane. Bead position was recorded every 90 milliseconds in bright field prior and during tether formation. Cells were maintained in the trap at 37$^{\circ C}$ and had CO_2 flowing into the chamber. Addition of CLEC-2 or CTRL supernatant was 2-4 hours prior to measurement of trap force. Trap force (F_t - pN/µm) was then calculated based on the trap calibration (k), bead position (δx) using a home-made Fiji macro (37) and the equation F_t=kδx.

Osmotic shock assay. Osmotic shock was performed in accordance with previously reported protocols (48). By altering the osmolarity of a solution cells will swell or shrink. Osmolarity was estimated using osmolarity calculations. Isotonic solution was prepared with 137mM NaCl, 5.4mM KCl, 1.8mM $CaCl_2$, 0.8mM $MgCl_2$, 20mM HEPES, 20mM D-glucose and pH to 7.4 with NaOH. Hypotonic (Hypo) solutions were prepared by diluting the isotonic preparation in milliq water i.e. 50 mOsm is a 1/6 dilution of Iso. To control for the dilution of ions in solution and account for the effect this may have on swelling, the 50 mOsm solution was restored to 330mOsm using D-mannitol at 280mM, acting as the true isotonic control (Iso). Cells were dissociated from cell culture with Sterile Dulbecco's phosphate buffered saline (DPBS) (Thermo Fischer scientific) + 2mM EDTA and placed onto individual 35mm MatTek dishes and allowed to settle for 30 minutes. After 30 minutes the cells remain rounded on the coverslip. Cells were then treated with either Iso, Hypo 50mOsm or Extreme Hypo 0mOsm for one hour. Phase contrast images of cell swelling were captured every 30 seconds using 20x air objective on a Nikon Ti inverted microscope with a motorised stage controlled by NIS-elements software. Diameter of individual swelling cells were calculated using manual circular ROIs. The ratio of swelling was then calculated by dividing all diameters (d) by the initial diameter (d_0). Area under the curves were calculated for the first 20 minutes of the swelling response.

Western Blotting. Equal cell numbers were grown to confluency and protein was isolated using 300µl of 4x Laemmlli Lysis Buffer (Bio-Rad) and cell lifters (Fisher Scientific). Lysates were then sonicated for 20 seconds followed by 10 minutes at 95$^{\circ C}$. 1% β-mercaptoethanol (143mM stock, Sigma Aldrich) was applied to samples to reduce oligomerised protein structures. Electrophoresis gels were loaded with the same quantity of lysates and run for 60 minutes at 110v. Transfer to PDVF membranes were carried out at 65v for 2hr at 4$^{\circ C}$. Membranes were blocked for 2hrs at room temperature with 5% skim milk powder (Sigma-Aldrich), 1% BSA in TBS and stained with primary antibodies (Antibody Table 1) overnight at 4$^{\circ C}$ in 1:5 diluted blocking buffer. Membranes were then washed thoroughly with TBS 0.05% Tween 20 and incubated with HRP-conjugated secondary antibodies (Antibody Table 1) in 1:5 blocking buffer. After washing with TBS 0.05% Tween 20. The membranes were visualised using ECL-HRP reaction and imaged using Image Quant 5000 (GE Lifesceinces).

Image analysis. Confocal images were processed in ImageJ. For analysis of PDPN, pMLC and Actin enrichment during acute inflammation of lymph nodes a home-made macro was used (Supplementary macro 1). Briefly images were split and whole image fluorescent intensities were determined (PDPN data). The $PDPN^+$ FRC network was identified by segmenting the PDPN stained structures in the image. The image was de-speckled and had outliers removed (radius= 5, threshold = 50, which=bright). Then a Gaussian blur was applied (sigma=2). Following this, images had a threshold applied (10,255) and a segmented mask generated. This mask was then applied to F-actin and pMLC channels to determine the intensities of these labels within the $PDPN^+$ FRC network. Enrichment scores were generated by comparing the amount of F-actin or pMLC fluorescence within the $PDPN^+$ network compared to the entire image. These scores were then normalised to the average enrichment score within steady state FRC networks. Rendering of PDPN in Figure 1E was achieved using Imaris surface tools.

Statistical analysis. Prism7 Software (GraphPad) was used to perform multiple statistical analyses including appropriate tests were performed as indicated in figure legends. In general, comparison of multiple groups was performed using Two-way ANOVA with Tukey's multiple comparisons or One-way ANOVA with Kruskal-Wallis test depending on the distribution of the data. Comparisons of two data sets were most performed using Two-tailed Mann-Whitley tests.

Bibliography

1. C.-Y. Yang, Tobias K Vogt, Stéphanie Favre, Leonardo Scarpellino, H.-Y. Huang, Fabienne Tacchini-Cottier, and Sanjiv A Luther. Trapping of naive lymphocytes triggers rapid growth and remodeling of the fibroblast network in reactive murine lymph nodes. *Proceedings of the National Academy of Sciences*, 111(1):E109–E118, 2014. ISSN 0027-8424. doi: 10.1073/pnas.1312585111.
2. Deepali Malhotra, Anne L. Fletcher, Jillian Astarita, Veronika Lukacs-Kornek, Prakriti Tayalia, Santiago F. Gonzalez, Kutlu G. Elpek, Sook Kyung Chang, Konstantin Knoblich, Martin E. Hemler, Michael B. Brenner, Michael C. Carroll, David J. Mooney, Shannon J. Turley, Yan Zhou, Susan A. Shinton, Richard R. Hardy, Natalie A. Bezman, Joseph C. Sun, Charlie C. Kim, Lewis L. Lanier, Jennifer Miller, Brian Brown, Miriam Merad, Angelique Bellemare-Pelletier, Kavitha Narayan, Katelyn Sylvia, Joonsoo Kang, Roi Gazit, Brian Garrison, Derrick J. Rossi, Vladimir Jojic, Daphne Koller, Radu Jianu, David Laidlaw, James Costello, Jim Collins, Nadia Cohen, Patrick Brennan, Tal Shay, Aviv Regev, Francis Kim, Tata Nageswara Rao, Amy Wagers, Emmanuel L. Gautier, Claudia Jakubzick, Gwendalyn J. Randolph, Paul Monach, Adam J. Best, Jamie Knell, Ananda Goldrath, Tracy Heng, Taras Kreslavsky, Michio Painter, Diane Mathis, and Christophe Benoist. Transcriptional profiling of stroma from inflamed and resting lymph nodes defines immunological hallmarks. *Nature Immunology*, 13(5):499–510, may 2012. ISSN 15292908. doi: 10.1038/ni.2262.
3. Anne L Fletcher, Sophie E Acton, and Konstantin Knoblich. Lymph node fibroblastic reticular cells in health and disease, 2015. ISSN 14741741.
4. Akshay T. Krishnamurty and Shannon J. Turley. Lymph node stromal cells: cartographers of the immune system, apr 2020. ISSN 15292916.
5. Alexander Link, Tobias K Vogt, Stéphanie Favre, Mirjam R Britschgi, Hans Acha-Orbea, Boris Hinz, Jason G Cyster, and Sanjiv A Luther. Fibroblastic reticular cells in lymph nodes regulate the homeostasis of naive T cells. *Nature Immunology*, 8(11):1255–1265, 2007. ISSN 15292908. doi: 10.1038/ni1513.
6. Lauren B. Rodda, Erick Lu, Mariko L. Bennett, Caroline L. Sokol, Xiaoming Wang, Sanjiv A. Luther, Ben A. Barres, Andrew D. Luster, Chun Jimmie Ye, and Jason G. Cyster. Single-Cell RNA Sequencing of Lymph Node Stromal Cells Reveals Niche-Associated Heterogeneity. *Immunity*, 48(5):1014–1028.e6, may 2018. ISSN 1074-7613. doi: 10.1016/J.IMMUNI.2018.04.006.
7. Christian Perez-Shibayama, Cristina Gil-Cruz, and Burkhard Ludewig. Fibroblastic reticular cells at the nexus of innate and adaptive immune responses, 2019. ISSN 1600065X.
8. Marc Bajénoff, Jackson G. Egen, Lily Y. Koo, Jean Pierre Laugier, Frédéric Brau, Nicolas Glaichenhaus, and Ronald N. Germain. Stromal Cell Networks Regulate Lymphocyte Entry, Migration, and Territoriality in Lymph Nodes. *Immunity*, 25(6):989–1001, dec 2006. ISSN 10747613. doi: 10.1016/j.immuni.2006.10.011.
9. Mario Novkovic, Lucas Onder, Jovana Cupovic, Jun Abe, David Bomze, Viviana Cremasco, Elke Scandella, Jens V. Stein, Gennady Bocharov, Shannon J. Turley, and Burkhard Ludewig. Topological Small-World Organization of the Fibroblastic Reticular Cell Network Determines Lymph Node Functionality. *PLoS Biology*, 14(7):1–20, 2016. ISSN 15457885. doi: 10.1371/journal.pbio.1002515.
10. Victor G Martinez, Valeriya Pankova, Lukas Krasny, Paul H Huang, Christopher J Tape, Sophie E Acton, Victor G Martinez, Valeriya Pankova, Lukas Krasny, Tanya Singh, Spyridon Makris, and Ian J White. Fibroblastic Reticular Cells Control Conduit Matrix Deposition during Lymph Node Expansion Article Fibroblastic Reticular Cells Control Conduit Matrix Deposition during Lymph Node Expansion. *CellReports*, 29(9):2810–2822.e5, 2019. ISSN 2211-1247. doi: 10.1016/j.celrep.2019.10.103.
11. Dominik Eder, Christof Aegerter, and Konrad Basler. Forces controlling organ growth and size, 2017. ISSN 18726356.
12. Tom Wyatt, Buzz Baum, and Guillaume Charras. A question of time: Tissue adaptation to mechanical forces, feb 2016. ISSN 18790410.
13. Carlos F. Guimarães, Luca Gasperini, Alexandra P. Marques, and Rui L. Reis. The stiffness of living tissues and its implications for tissue engineering. *Nature Reviews Materials*, 5(5): 351–370, 2020. ISSN 20588437. doi: 10.1038/s41578-019-0169-1.
14. Yanlan Mao and Buzz Baum. Tug of war-The influence of opposing physical forces on epithelial cell morphology, may 2015. ISSN 1095564X.
15. Benoit Ladoux and René Marc Mège. Mechanobiology of collective cell behaviours. *Nature Reviews Molecular Cell Biology*, 18(12):743–757, dec 2017. ISSN 14710080. doi: 10.1038/nrm.2017.98.
16. Sophie E. Acton, Aaron J. Farrugia, Jillian L. Astarita, Diego Mourão-Sá, Robert P. Jenkins, Emma Nye, Steven Hooper, Janneke Van Blijswijk, Neil C. Rogers, Kathryn J. Snelgrove, Ian Rosewell, Luis F. Moita, Gordon Stamp, Shannon J. Turley, Erik Sahai, and Caetano Reise Sousa. Dendritic cells control fibroblastic reticular network tension and lymph node expansion. *Nature*, 514(7253):498–502, 2014. ISSN 14764687. doi: 10.1038/nature13814.
17. Jillian L Astarita, Viviana Cremasco, Jianxin Fu, Max C Darnell, James R Peck, Janice M Nieves-Bonilla, Kai Song, Yuji Kondo, Matthew C Woodruff, Alvin Gogineni, Lucas Onder, Burkhard Ludewig, Robby M Weimer, Michael C Carroll, David J Mooney, Lijun Xia, and Shannon J Turley. The CLEC-2-podoplanin axis controls the contractility of fibroblastic reticular cells and lymph node microarchitecture. *Nature Immunology*, 16(1):75–84, 2015. ISSN 15292916. doi: 10.1038/ni.3035.
18. Guillaume Salbreux, Guillaume Charras, and Ewa Paluch. Actin cortex mechanics and cellular morphogenesis. *Trends in Cell Biology*, 22(10):536–545, 2012. ISSN 09628924. doi: 10.1016/j.tcb.2012.07.001.
19. Thomas Lecuit and Pierre François Lenne. Cell surface mechanics and the control of cell shape, tissue patterns and morphogenesis, aug 2007. ISSN 14710072.
20. Qian Chai, Lucas Onder, Elke Scandella, Cristina Gil-Cruz, Christian Perez-Shibayama, Jovana Cupovic, Renzo Danuser, Tim Sparwasser, Sanjiv A Luther, Volker Thiel, Thomas Rülicke, Jens V Stein, Thomas Hehlgans, and Burkhard Ludewig. Maturation of Lymph Node Fibroblastic Reticular Cells from Myofibroblastic Precursors Is Critical for Antiviral Immunity. *Immunity*, 38(5):1013–1024, 2013. ISSN 10747613. doi: 10.1016/j.immuni.2013.03.012.
21. Jillian L Astarita, Sophie E Acton, and Shannon J Turley. Podoplanin: Emerging functions in development, the immune system, and cancer, 2012. ISSN 16643224.
22. Saikat Majumder, Nilesh Amatya, Shankar Revu, Chetan V Jawale, Dongwen Wu, Natalie Rittenhouse, Ashley Menk, Saran Kupul, Fang Du, Itay Raphael, Amrita Bhattacharjee, Ulrich Siebenlist, Timothy W Hand, Greg M Delgoffe, Amanda C Poholek, Sarah L Gaffen, Partha S Biswas, and Mandy J McGeachy. IL-17 metabolically reprograms activated fibroblastic reticular cells for proliferation and survival. *Nature Immunology*, 20(5):534–545, 2019. ISSN 15292916. doi: 10.1038/s41590-019-0367-4.
23. Marc Bajénoff, Nicolas Glaichenhaus, and Ronald N. Germain. Fibroblastic Reticular Cells Guide T Lymphocyte Entry into and Migration within the Splenic T Cell Zone. *The Journal of Immunology*, 181(6):3947–3954, 2008. ISSN 0022-1767. doi: 10.4049/jimmunol.181.6.3947.
24. Brett H Herzog, Jianxin Fu, Stephen J Wilson, Paul R Hess, Aslihan Sen, J. Michael McDaniel, Yanfang Pan, Minjia Sheng, Tadayuki Yago, Robert Silasi-Mansat, Samuel McGee, Frauke May, Bernhard Nieswandt, Andrew J Morris, Florea Lupu, Shaun R Coughlin, Rodger P. McEver, Hong Chen, Mark L Kahn, and Lijun Xia. Podoplanin maintains high endothelial venule integrity by interacting with platelet CLEC-2. *Nature*, 502(7469):105–109, 2013. ISSN 00280836. doi: 10.1038/nature12501.
25. Viviana Cremasco, Matthew C Woodruff, Lucas Onder, Jovana Cupovic, Janice M Nieves-Bonilla, Frank A Schildberg, Jonathan Chang, Floriana Cremasco, Christopher J Harvey, Kai Wucherpfennig, Burkhard Ludewig, Michael C Carroll, and Shannon J Turley. B cell homeostasis and follicle confines are governed by fibroblastic reticular cells. *Nature Immunology*, 15(10):973–981, 2014. ISSN 15292916. doi: 10.1038/ni.2965.
26. Michael Sixt, Nobuo Kanazawa, Manuel Selg, Thomas Samson, Gunnel Roos, Dieter P. Reinhardt, Reinhard Pabst, Manfred B. Lutz, and Lydia Sorokin. The conduit system transports soluble antigens from the afferent lymph to resident dendritic cells in the T cell area of the lymph node. *Immunity*, 22(1):19–29, jan 2005. ISSN 10747613. doi: 10.1016/j.immuni.2004.11.013.
27. Charlotte M De Winde, Spyridon Makris, Lindsey Millward, Jesús Cantoral Rebordinos, Agnesska C Benjamin, Víctor G Martínez, and Sophie E Acton. Fibroblastic Reticular Cell Response to Dendritic Cells Requires Coordinated Activity of Podoplanin, CD44 and CD9. doi: 10.1101/793141.
28. Jocelyn Étienne, Jonathan Fouchard, Démosthène Mitrossilis, Nathalie Bufi, Pauline Durand-Smet, and Atef Asnacios. Cells as liquid motors: Mechanosensitivity emerges from collective dynamics of actomyosin cortex. *Proceedings of the National Academy of Sciences of the United States of America*, 112(9):2740–2745, 2015. ISSN 10916490. doi: 10.1073/pnas.1417113112.
29. Manuel Théry, Victor Racine, Anne Pépin, Matthieu Piel, Yong Chen, Jean Baptiste Sibarita, and Michel Bornens. The extracellular matrix guides the orientation of the cell division axis. *Nature Cell Biology*, 7(10):947–953, 2005. ISSN 14657392. doi: 10.1038/ncb1307.
30. Manuel Théry, Anne Pépin, Emilie Dressaire, Yong Chen, and Michel Bornens. Cell distribution of stress fibres in response to the geometry of the adhesive environment. *Cell Motility and the Cytoskeleton*, 63(6):341–355, 2006. ISSN 08861544. doi: 10.1002/cm.20126.
31. Reza Farhadifar, Jens Christian Röper, Benoit Aigouy, Suzanne Eaton, and Frank Jülicher. The Influence of Cell Mechanics, Cell-Cell Interactions, and Proliferation on Epithelial Packing. *Current Biology*, 17(24):2095–2104, 2007. ISSN 09609822. doi: 10.1016/j.cub.2007.11.049.
32. Maria Duda, Natalie J Kirkland, Nargess Khalilgharibi, Melda Tozluoglu, Alice C. Yuen, Nicolas Carpi, Anna Bove, Matthieu Piel, Guillaume Charras, Buzz Baum, and Yanlan Mao. Polarization of Myosin II Refines Tissue Material Properties to Buffer Mechanical Stress. *Developmental Cell*, 48(2):245–260.e7, 2019. ISSN 18781551. doi: 10.1016/j.devcel.2018.12.020.
33. Robert J Tetley, Michael F Staddon, Davide Heller, Andreas Hoppe, Shiladitya Banerjee, and Yanlan Mao. Tissue fluidity promotes epithelial wound healing. *Nature Physics*, 2019. ISSN 1745-2473. doi: 10.1038/s41567-019-0618-1.
34. Jeffrey B. Wyckoff, Sophie E. Pinner, Steve Gschmeissner, John S. Condeelis, and Erik Sahai. ROCK- and Myosin-Dependent Matrix Deformation Enables Protease-Independent Tumor-Cell Invasion In Vivo. *Current Biology*, 16(15):1515–1523, 2006. ISSN 09609822. doi: c.
35. Bruno Pontes, Pascale Monzo, Laurent Gole, Anabel Lise Le Roux, Anita Joanna Kosmalska, Zhi Yang Tam, Weiwei Luo, Sophie Kan, Virgile Viasnoff, Pere Roca-Cusachs, Lisa Tucker-Kellogg, and Nils C. Gauthier. Membrane tension controls adhesion positioning at the leading edge of cells. *Journal of Cell Biology*, 216(9):2959–2977, sep 2017. ISSN 15408140. doi: 10.1083/jcb.201611117.
36. Alba Diz-Muñoz, Kevin Thurley, Sana Chintamen, Steven J Altschuler, Lani F Wu, Daniel A Fletcher, and Orion D Weiner. Membrane Tension Acts Through PLD2 and mTORC2 to Limit Actin Network Assembly During Neutrophil Migration. *PLoS Biology*, 14(6), 2016. ISSN 15457885. doi: 10.1371/journal.pbio.1002474.
37. Henry De Belly, Aki Stubb, Ayaka Yanagida, Céline Labouesse, Philip H. Jones, Ewa K. Paluch, and Kevin J. Chalut. Membrane Tension Gates ERK-Mediated Regulation of Pluripotent Cell Fate. *Cell Stem Cell*, 28(2):273–284.e6, feb 2021. ISSN 18759777. doi: 10.1016/j.stem.2020.10.018.
38. Arnon D Lieber, Shlomit Yehudai-Resheff, Erin L Barnhart, Julie A Theriot, and Kinneret

Keren. Membrane tension in rapidly moving cells is determined by cytoskeletal forces. *Current Biology*, 23(15):1409–1417, 2013. ISSN 09609822. doi: 10.1016/j.cub.2013.05.063.

39. J. Dai and M. P. Sheetz. Mechanical properties of neuronal growth cone membranes studied by tether formation with laser optical tweezers. *Biophysical Journal*, 68(3):988–996, 1995. ISSN 00063495. doi: 10.1016/S0006-3495(95)80274-2.
40. Ester Martín-Villar, Francisco G. Scholl, Carlos Gamallo, Maria M. Yurrita, Mario Muñoz-Guerra, Jesús Cruces, and Miguel Quintanilla. Characterization of human PA2.26 antigen (T1α-2, podoplanin), a small membrane mucin induced in oral squamous cell carcinomas. *International Journal of Cancer*, 113(6):899–910, mar 2005. ISSN 00207136. doi: 10.1002/ijc.20656.
41. E. Martin-Villar, D. Megias, Susanna Castel, Maria Marta Yurrita, S. Vilaro, and Miguel Quintanilla. Podoplanin binds ERM proteins to activate RhoA and promote epithelial-mesenchymal transition. *Journal of Cell Science*, 119(21):4541–4553, nov 2006. ISSN 0021-9533. doi: 10.1242/jcs.03218.
42. Beatriz Fernández-Muñoz, María M. Yurrita, Ester Martín-Villar, Patricia Carrasco-Ramírez, Diego Megías, Jaime Renart, and Miguel Quintanilla. The transmembrane domain of podoplanin is required for its association with lipid rafts and the induction of epithelial-mesenchymal transition. *International Journal of Biochemistry and Cell Biology*, 43(6):886–896, jun 2011. ISSN 13572725. doi: 10.1016/j.biocel.2011.02.010.
43. Bruno Pontes, Pascale Monzo, and Nils C. Gauthier. Membrane tension: A challenging but universal physical parameter in cell biology, nov 2017. ISSN 10963634.
44. Joshua H Bourne, Nonantzin Beristain-Covarrubias, Malou Zuidscheroude, Joana Campos, Ying Di, Evelyn Garlick, Martina Colicchia, Lauren V Terry, Steven G Thomas, Alexander Brill, Jagadeesh Bayry, Steve P Watson, and Julie Rayes. CLEC-2 promotes inflammatory peritoneal macrophage emigration to draining lymph nodes during endotoxemia. doi: 10.1101/2020.12.21.423770.
45. Harini Krishnan, Jhon A Ochoa-Alvarez, Yongquan Shen, Evan Nevel, Meenakshi Lakshminarayanan, Mary C Williams, Maria I Ramirez, W Todd Miller, and Gary S Goldberg. Serines in the intracellular tail of podoplanin (PDPN) regulate cell motility. *Journal of Biological Chemistry*, 288(17):12215–12221, 2013. ISSN 00219258. doi: 10.1074/jbc.C112.446823.
46. J E Gretz, a O Anderson, and S Shaw. Cords, channels, corridors and conduits: critical architectural elements facilitating cell interactions in the lymph node cortex. *Immunological reviews*, 156:11–24, 1997. ISSN 0105-2896. doi: 10.1111/j.1600-065X.1997.tb00955.x.
47. Enrico Crivellato and Franco Mallardi. Stromal cell organisation in the mouse lymph node. A light and electron microscopic investigation using the zinc iodide-osmium technique. *Journal of Anatomy*, 190(1):85–92, 1997. ISSN 00218782. doi: 10.1017/S0021878296001501.
48. Vincent Compan, Alberto Baroja-Mazo, Gloria López-Castejón, Ana I Gomez, Carlos M Martínez, Diego Angosto, María T Montero, Antonio S Herranz, Eulalia Bazán, Diana Reimers, Victoriano Mulero, and Pablo Pelegrín. Cell Volume Regulation Modulates NLRP3 Inflammasome Activation. *Immunity*, 37(3):487–500, 2012. ISSN 10747613. doi: 10.1016/j.immuni.2012.06.013.
49. Clotilde Cadart, Larisa Venkova, Pierre Recho, Marco Cosentino Lagomarsino, and Matthieu Piel. The physics of cell-size regulation across timescales. *Nature Physics*, 2019. ISSN 1745-2473. doi: 10.1038/s41567-019-0629-y.
50. Ewa Zlotek-Zlotkiewicz, Sylvain Monnier, Giovanni Cappello, Mael Le Berre, and Matthieu Piel. Optical volume and mass measurements show that mammalian cells swell during mitosis. *Journal of Cell Biology*, 211(4):765–774, 2015. ISSN 15408140. doi: 10.1083/jcb.201505056.
51. Sophie E. Acton, Jillian L. Astarita, Deepali Malhotra, Veronika Lukacs-Kornek, Bettina Franz, Paul R. Hess, Zoltan Jakus, Michael Kuligowski, Anne L. Fletcher, Kutlu G. Elpek, Angelique Bellemare-Pelletier, Lindsay Sceats, Erika D. Reynoso, Santiago F. Gonzalez, Daniel B. Graham, Jonathan Chang, Anneli Peters, Matthew Woodruff, Young A. Kim, Wojciech Swat, Takashi Morita, Vijay Kuchroo, Michael C. Carroll, Mark L. Kahn, Kai W. Wucherpfennig, and Shannon J. Turley. Podoplanin-Rich Stromal Networks Induce Dendritic Cell Motility via Activation of the C-type Lectin Receptor CLEC-2. *Immunity*, 37(2):276–289, 2012. ISSN 10747613. doi: 10.1016/j.immuni.2012.05.022.
52. Julia L Gregory, Anne Walter, Yannick O Alexandre, Jyh Liang Hor, Ruijie Liu, Joel Z. Ma, Sapna Devi, Nobuko Tokuda, Yuji Owada, Laura K. Mackay, Gordon K Smyth, William R Heath, and Scott N. Mueller. Infection Programs Sustained Lymphoid Stromal Cell Responses and Shapes Lymph Node Remodeling upon Secondary Challenge. *Cell Reports*, 18(2):406–418, 2017. ISSN 22111247. doi: 10.1016/j.celrep.2016.12.038.
53. Victoria Sanz-Moreno, Gilles Gadea, Jessica Ahn, Hugh Paterson, Pierfrancesco Marra, Sophie Pinner, Erik Sahai, and Christopher J. Marshall. Rac Activation and Inactivation Control Plasticity of Tumor Cell Movement. *Cell*, 135(3):510–523, 2008. ISSN 00928674. doi: 10.1016/j.cell.2008.09.043.
54. S A Gudipaty, J Lindblom, P D Loftus, M. J. Redd, K Edes, C. F. Davey, V Krishnegowda, and J. Rosenblatt. Mechanical stretch triggers rapid epithelial cell division through Piezo1. *Nature*, 543(7643):118–121, 2017. ISSN 14764687. doi: 10.1038/nature21407.
55. Sean Porazinski, Huijia Wang, Yoichi Asaoka, Martin Behrndt, Tatsuo Miyamoto, Hitoshi Morita, Shoji Hata, Takashi Sasaki, S. F.Gabriel Krens, Yumi Osada, Satoshi Asaka, Akihiro Momoi, Sarah Linton, Joel B. Miesfeld, Brian A. Link, Takeshi Senga, Atahualpa Castillo-Morales, Araxi O. Urrutia, Nobuyoshi Shimizu, Hideaki Nagase, Shinya Matsuura, Stefan Bagby, Hisato Kondoh, Hiroshi Nishina, Carl Philipp Heisenberg, and Makoto Furutani-Seiki. YAP is essential for tissue tension to ensure vertebrate 3D body shape. *Nature*, 521(7551):217–221, may 2015. ISSN 14764687. doi: 10.1038/nature14215.
56. Marina Uroz, Sabrina Wistorf, Xavier Serra-Picamal, Vito Conte, Marta Sales-Pardo, Pere Roca-Cusachs, Roger Guimerà, and Xavier Trepat. Regulation of cell cycle progression by cell–cell and cell–matrix forces. *Nature Cell Biology*, page 1, 2018. ISSN 1465-7392. doi: 10.1038/s41556-018-0107-2.
57. Jonathan E Chang, Matthew B Buechler, Elise Gressier, Shannon J Turley, and Michael C Carroll. Mechanosensing by Peyer's patch stroma regulates lymphocyte migration and mucosal antibody responses. *Nature Immunology*, 20(11):1506–1516, 2019. ISSN 15292916. doi: 10.1038/s41590-019-0505-z.
58. Sung Yong Choi, Hosung Bae, Sun Hye Jeong, Intae Park, Hyunsoo Cho, Seon Pyo Hong, Da Hye Lee, Choong kun Lee, Jin Sung Park, Sang Heon Suh, Jeongwoon Choi, Myung Jin Yang, Jeon Yeob Jang, Lucas Onder, Jeong Hwan Moon, Han Sin Jeong, Ralf H Adams, Jin Man Kim, Burkhard Ludewig, Joo Hye Song, Dae Sik Lim, and Gou Young Koh. YAP/TAZ direct commitment and maturation of lymph node fibroblastic reticular cells. *Nature Communications*, 11(1), 2020. ISSN 20411723. doi: 10.1038/s41467-020-14293-1.
59. Fatemeh S. Majedi, Mohammad Mahdi Hasani-Sadrabadi, Timothy J. Thauland, Song Li, Louis S. Bouchard, and Manish J. Butte. T-cell activation is modulated by the 3D mechanical microenvironment. *Biomaterials*, 252:120058, sep 2020. ISSN 18785905. doi: 10.1016/j.biomaterials.2020.120058.
60. Kevin P Meng, Fatemeh S Majedi, Timothy J Thauland, and Manish J Butte. Mechanosensing through YAP controls T cell activation and metabolism. *Journal of Experimental Medicine*, 217(8), 2020. ISSN 15409538. doi: 10.1084/jem.20200053.
61. Ziqing Liu, Olivia Chen, J. Blake Joseph Wall, Michael Zheng, Yang Zhou, Li Wang, Haley Ruth Vaseghi, Li Qian, and Jiandong Liu. Systematic comparison of 2A peptides for cloning multi-genes in a polycistronic vector. *Scientific Reports*, 7(1), 2017. ISSN 20452322. doi: 10.1038/s41598-017-02460-2.
62. Engin Bozdag. *Intravital Imaging of Dynamic Bone and Immune Systems*, volume 1763. 2018. ISBN 978-1-4939-7761-1. doi: 10.1007/978-1-4939-7762-8.
63. Benjamin D. Groff, Andrew W.L. Kinman, Jacob F. Woodroof, and Rebecca R. Pompano. Immunofluorescence staining of live lymph node tissue slices. *Journal of Immunological Methods*, 464:119–125, 2019. ISSN 18727905. doi: 10.1016/j.jim.2018.10.010.
64. Maura C. Belanger, Alexander G. Ball, Megan A. Catterton, Andrew W.L. Kinman, Parastoo Anbaei, Benjamin D. Groff, Stephanie J. Melchor, John R. Lukens, Ashley E. Ross, and Rebecca R. Pompano. Acute Lymph Node Slices Are a Functional Model System to Study Immunity Ex Vivo. *ACS Pharmacology and Translational Science*, 4(1):128–142, 2021. ISSN 25759108. doi: 10.1021/acsptsci.0c00143.
65. Yanlan Mao, Alexander L. Tournier, Andreas Hoppe, Lennart Kester, Barry J. Thompson, and Nicolas Tapon. Differential proliferation rates generate patterns of mechanical tension that orient tissue growth. *EMBO Journal*, 32(21):2790–2803, 2013. ISSN 02614189. doi: 10.1038/emboj.2013.197.
66. Anne L Fletcher, Deepali Malhotra, Sophie E Acton, Veronika Lukacs-Kornek, Angelique Bellemare-Pelletier, Mark Curry, Myriam Armant, and Shannon J Turley. Reproducible isolation of lymph node stromal cells reveals site-dependent differences in fibroblastic reticular cells. *Frontiers in Immunology*, 2(SEP), 2011. ISSN 16643224. doi: 10.3389/fimmu.2011.00035.

Supplementary Note 1: Supplementary Data

QR code for supplementary movies

Supplementary movies 1 – Tile scans of inguinal lymph nodes throughout inflammation
A-C) Movies zoom into two different T-cell FRC regions demonstrating the staining of the conduit (perlecan, magenta), FRC network (PDPN, yellow), F-actin (phalloidin, cyan) and pMLC (red).

Supplementary movies 2 – Zoomed regions of the T-cell FRC network, showing 3D localisation of actomyosin structures
A-C) Staining of the conduit (perlecan, magenta), FRC network (PDPN, yellow), F-actin (phalloidin, cyan) and pMLC (red). PDPN and perlecan surface renders show the location of actomyosin in relation to these structures.

Supplementary movie 3 – Live cell imaging of ablation of the FRC network demonstrates mechanical tension
A-C) GFP denotes the FRC network membrane. Movies captured over 25 seconds. Yellow line marks site of cut one second after imaging began.

Supplementary movie 4 – Optical tweezers generate membrane tethers used to determine membrane tension

Supplementary movie 5 – Osmotic swelling of fibroblastic reticular cells
A-D) Movies captured over 60 minutes with one frame every 30 seconds. A) PDPN CTRL + CLEC2 (left), PDPN CTRL – CLEC2 (middle), PDPN CTRL ISO control (right). B) PDPN T34A + CLEC2 (left), PDPN T34A – CLEC2 (middle), PDPN T34A ISO control (right). C) CTRL + HYPO (left), PDPN KD + HYPO (middle), CTRL ISO control (right). D) CTRL + H20 (left), PDPN KD + H20 (right)

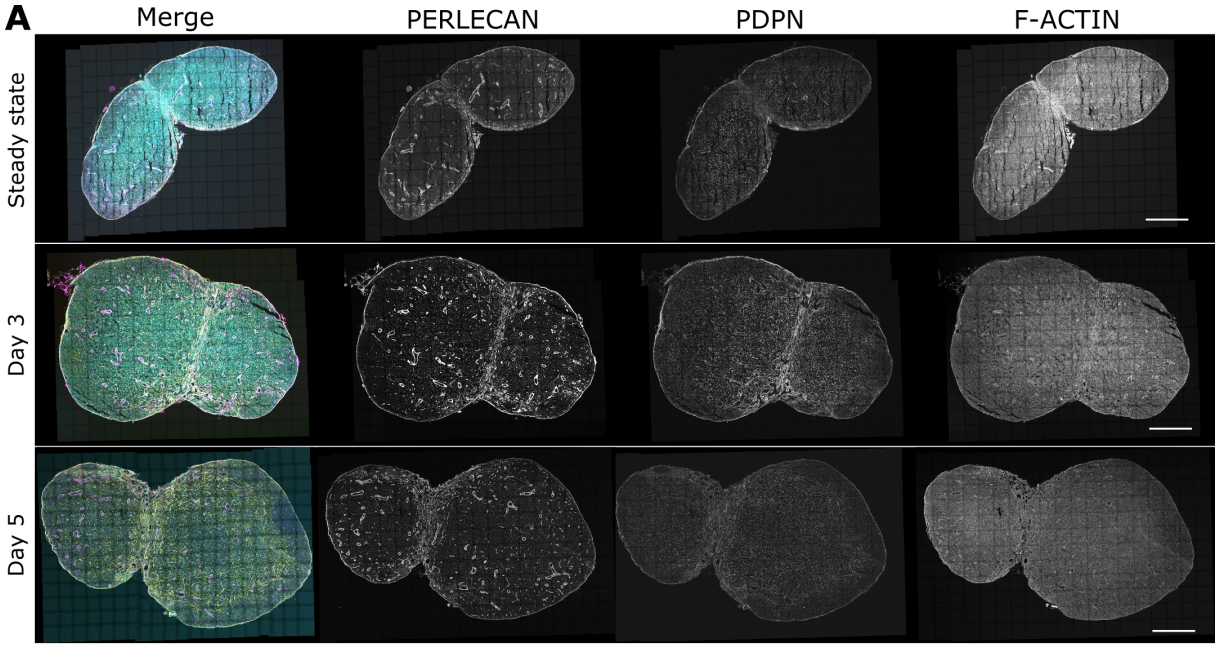

Fig. S1. Representative tile scans of pelecan, PDPN and F-actin staining throughout inflammation A) Representative tile scan of inguinal LN in the steady state and 3 or 5 days post IFA/OVA immunisation. Individual staining of perlecan (Conduit), PDPN (FRC-network) and phalloidin (F-actin). Scale bar 500µm.

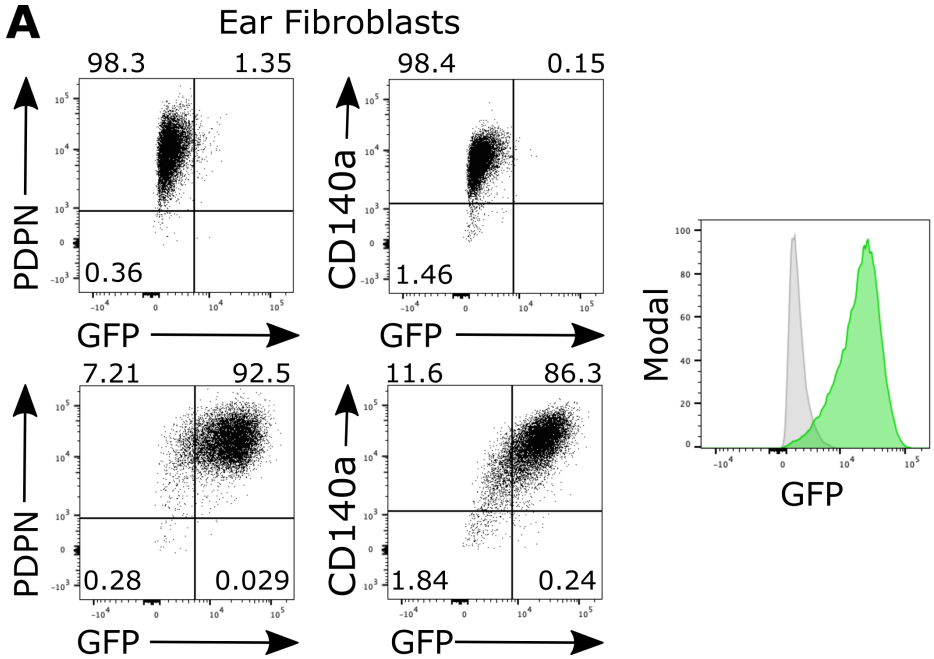

Fig. S2. Flow cytometry of PDGFRα-mGFP fibroblasts A) Flow cytometry panel of PDPN$^+$ and CD140α$^+$ skin fibroblasts expressing GFP.Top two panels show GFP$^-$ control fibroblasts. Bottom two panels show PDPN$^+$, GFP$^+$ and CD140α$^+$ GFP$^+$ fibroblasts. Right panel shows control fibroblasts (grey) to PDGFRα-mGFP fibroblasts (green).

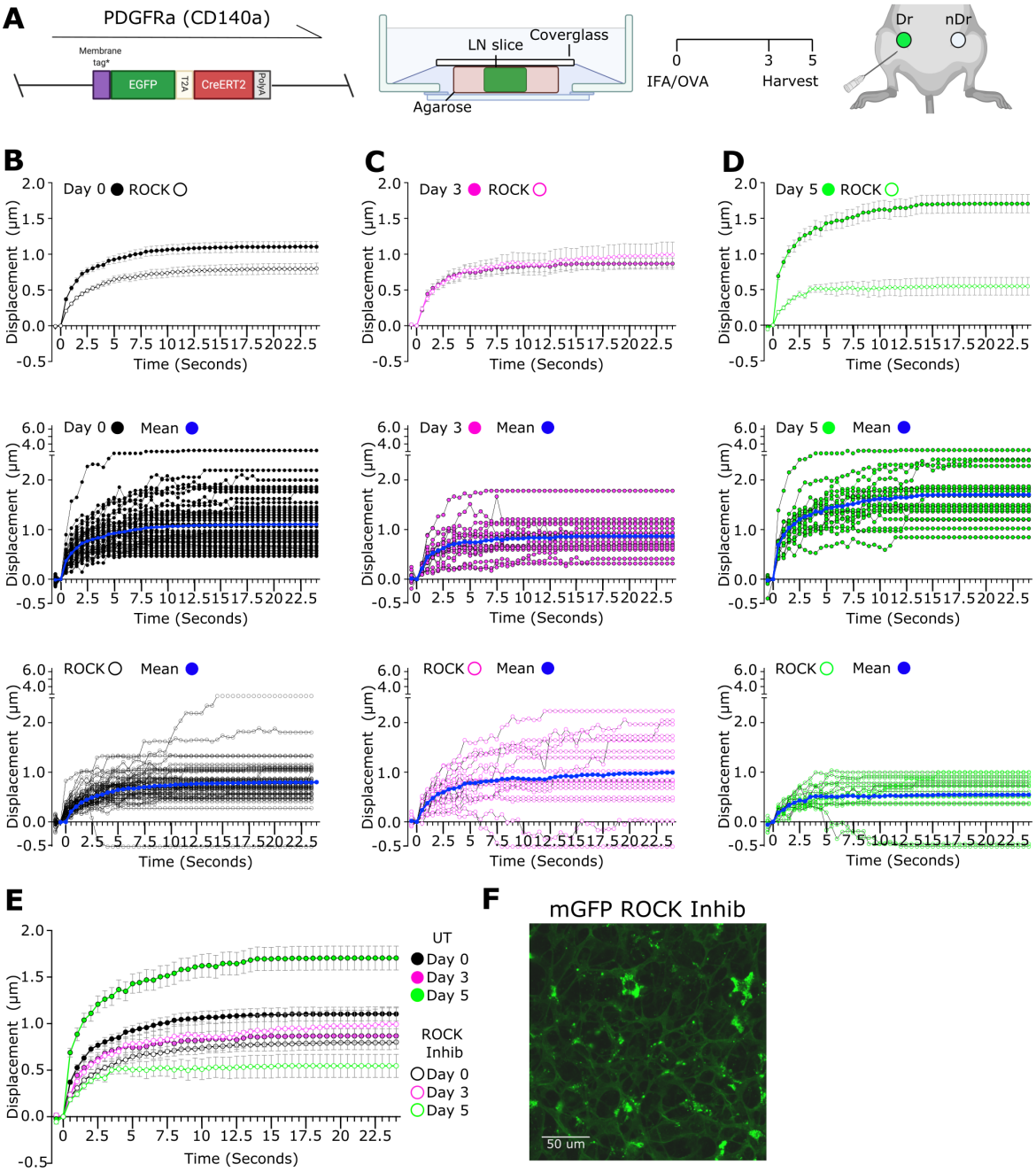

Fig. S3. Y27 treatment of lymph node slices reduce tension in the FRC network A) Schematic of immunisation and animal models. A membrane targeted GFP molecule is driven under the (PDGFRα) promoter (left). LN nodes were embedded in low melt agarose and sliced at 200µm thickness before being secured by cover glass for imaging (middle). IFA/OVA is used as model immunisation with inguinal lymph nodes (LN's) harvested day 3 or day 5 post immunisation (right). B-D) Recoil curves show displacement over time (mean ±SEM) (top panel). Individual recoil curves of control (middle) and Y27 treated LNs (bottom). N>5 animals per condition. E) Recoil curves show displacement over time (mean ±SEM), comparing untreated and Y27 treated LNs. Blue shading indicates initial recoil phase. N>5 animals per condition. F) Membrane GFP visualises the FRC network in the *ex vivo* lymph node slice. Y27 treatment has no effect on the FRC network connectivity. Scale bar 50µm.

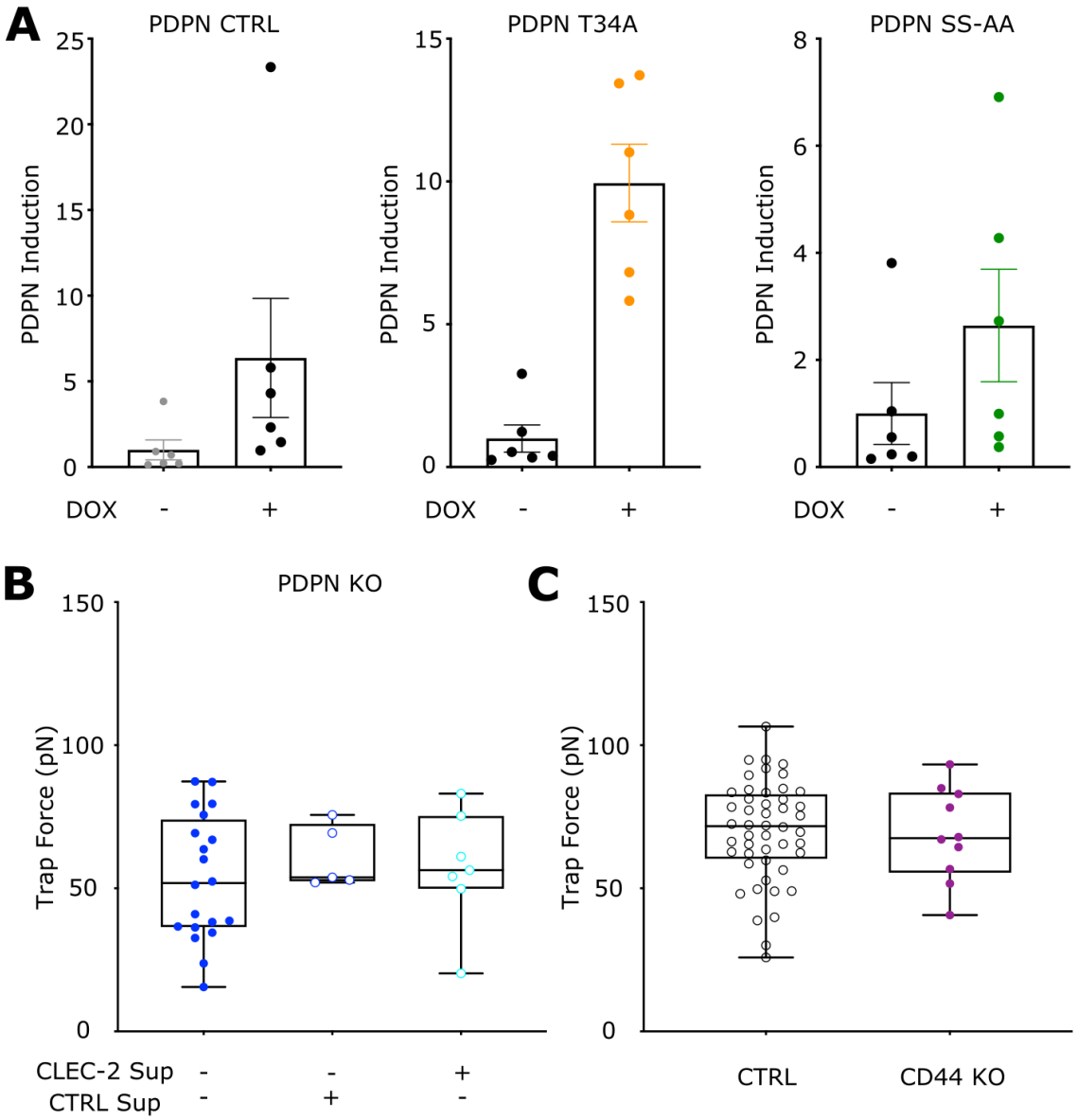

Fig. S4. Induction of PDPN mutants in PDPN KO fibroblastic reticular cell line A) Fold induction of PDPN geometric mean for PDPN mutants treated with or without doxycycline. PDPN CTRL (left), PDPN T34A (middle) and PDPN DSS (right). N=6. B) Trap force measurements of PDPN CRISPR KO FRCs treated with CTRL or CLEC-2 supernatant. One-way ANOVA with Tukeys multiple comparisons. N>5. C) Trap force measurements of CTRL and CD44 (purple) KO FRCs. Mann-Whitney test, p<0.001. Each point represents one cell. N>10

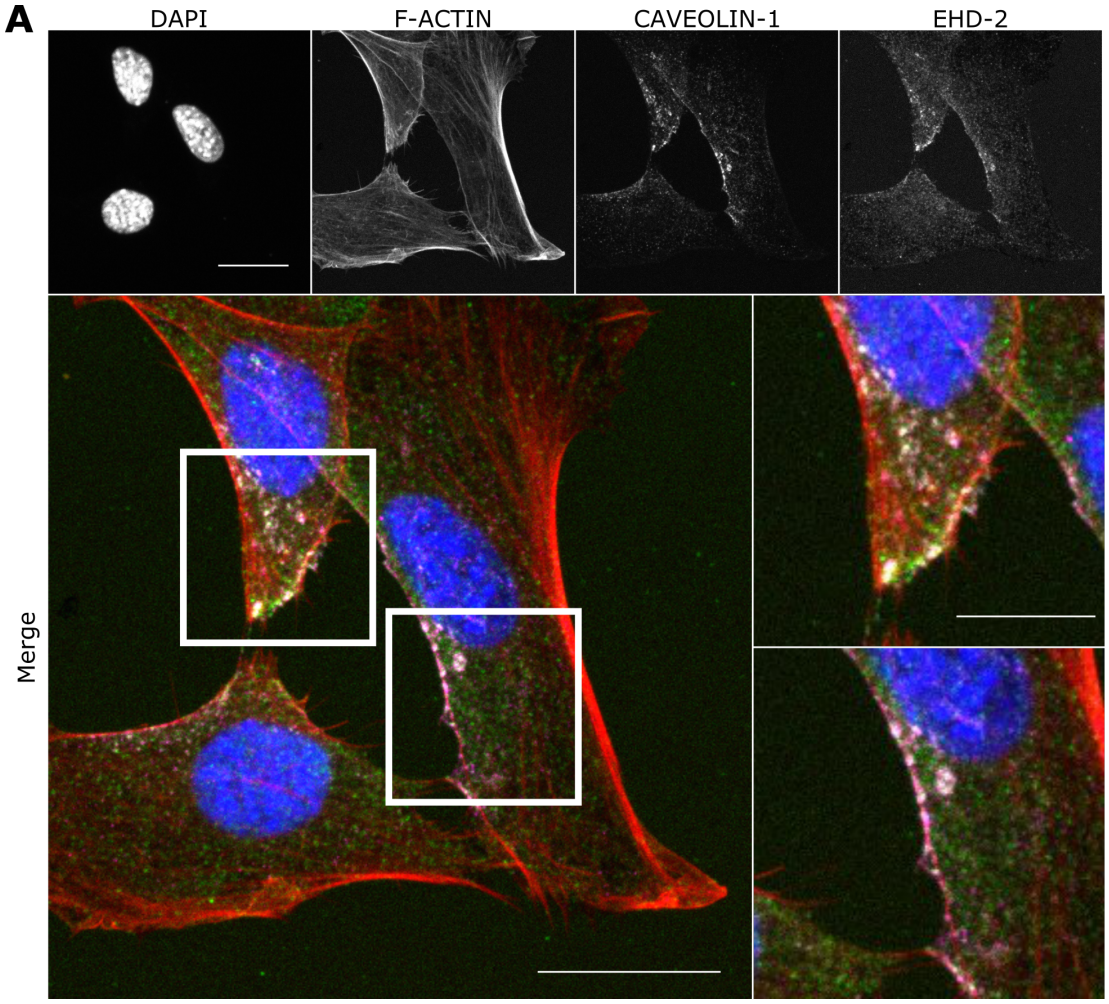

Fig. S5. FRCs contain active caveolae membrane stores A) Representative image of CTRL FRCs expressing caveolin 1 and colocalising with EHD2 to form active caveolae structures. Scale bar 20µm. White box indicates digital zooms highlighting the membrane stores. Merged image contains DAPI (Blue), F-actin (Red), Caveolin-1 (magenta) and EHD2 (Green). Scale bar 10µm.

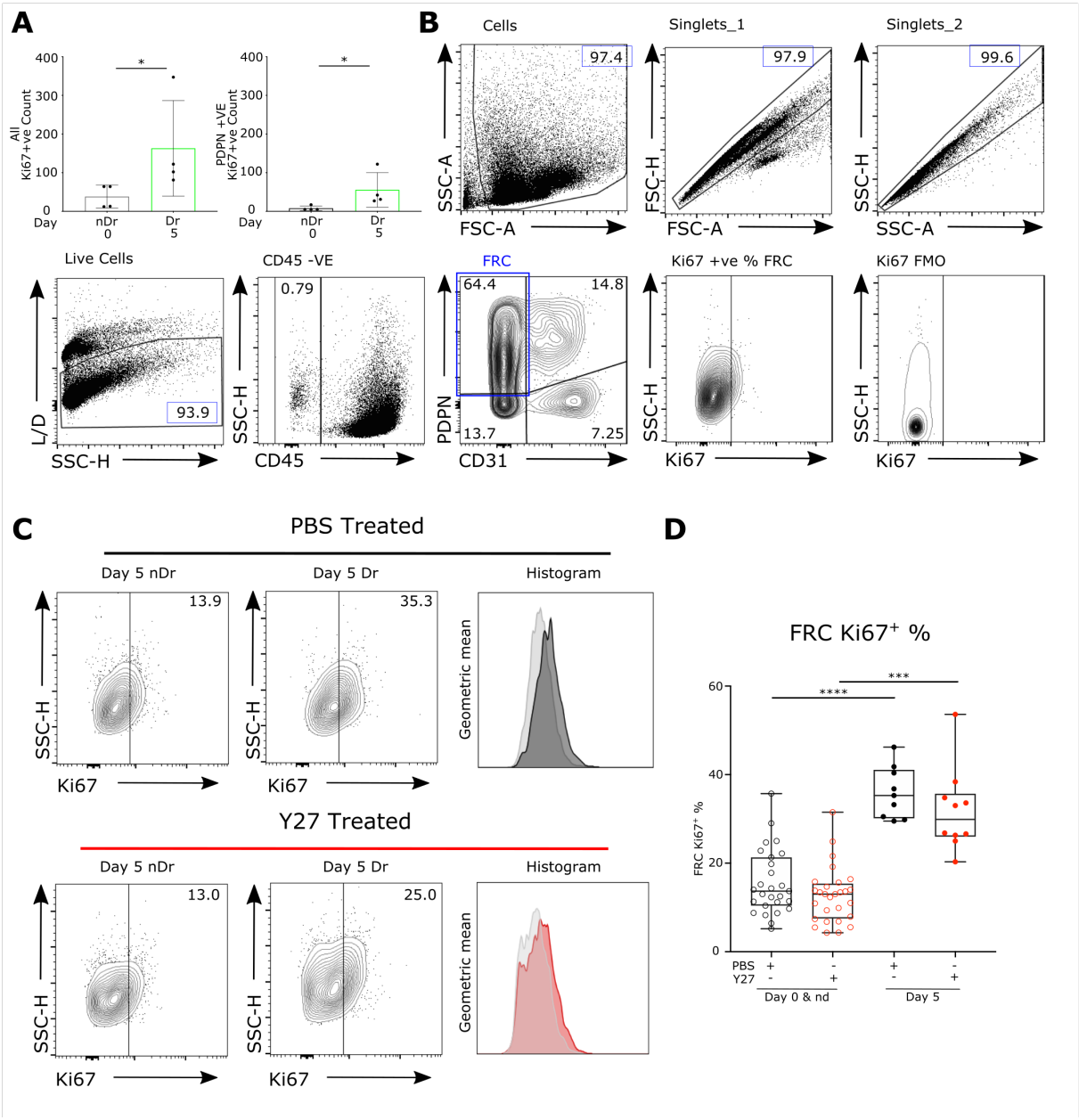

Fig. S6. Flow cytometry gating strategy and Ki67 measurements A) Quantification of Ki67$^+$ cells (top) and PDPN$^+$ Ki67$^+$ cells (bottom) per LN region. Box plots indicates median and interquartile range. Mann-Whitney test, $p<0.05$. N=2. B) Schema of flow cytometry gating strategy for measurement of stromal cell populations. C) Example of Ki67$^+$ FRCs cell plots and histogram of Ki67 geometric mean, comparing immunisation and Y27 treatments. D) Quantification of Ki67$^+$ FRCs. Box plots indicates median and interquartile range. Two-way ANOVA with Tukey's multiple comparisons. ****$p<0.0001$, ***$p<0.001$. N>9 animals per condition

Antibody	Species	Dilution	Manufacturer	Product ID
Alexa Fluor 405	Donkey anti-rat	1:500(IF)	abcam	ab175670
Alexa Fluor 488	Goat-Anti Rabbit	1:500 (IF)	Thermo Fischer Scientific	A-11034
Alexa Fluor 488	Goat-Anti Hamster	1:500 (IF)	Thermo Fischer Scientific	A-21110
Alexa Fluor 555	Goat-Anti Rabbit	1:500 (IF)	Thermo Fischer Scientific	A-21429
Alexa Fluor 594	Donkey-Anti rabbit	1:500 (IF)	Abcam	ab150076
Alexa Fluor 633 Phalloidin	Amanita phalloides	1:200 (IF), 1:500 (IF)	Thermo Fischer Scientific	A-22284
Alexa Fluor 647	Goat-Anti Rabbit	1:500 (IF)	Thermo Fischer Scientific	A-21245
Alexa Fluor 647	Goat-Anti Hamster	1:500 (IF)	Thermo Fischer Scientific	a-21451
Alexa Fluor 647	Goat-Anti Rat	1:500 (IF)	Thermo Fischer Scientific	A-21247
Anti-aggrus (Podoplanin) clone 8F11	Rat anti mouse	1:1000 (WB)	MBL international	D190-3
APC/Fire 750 cd31 [390]	Anti-mouse	1:100 (Flow)	BioLegend	102434
Brilliant Violet 750TM CD45	Anti-mouse	1:100 (Flow)	BioLegend	103157
BV421 MAdCAM-1 Clone MECA	Rat anti-mouse	1:100 (Flow)	BD	742812
Caveolin-1	Rabbit	1:1000 (IF)	Abcam	ab2910
DAPI		1:1000 (IF)	Sigma Aldrich	D9542-1MG
EHD2	Rabbit	1:500 (IF)	Abcam	ab23935
Histone H3	Mouse	1:2000 (WB)	Abcam	24834
HRP anti mouse	Rabbit anti mouse	1:10000 (WB)	Abcam	ab6728
HRP anti Rabbit	Goat anti rabbite	1:15000 (WB)	Abcam	ab6721
HRP anti Rat	Rabbit anti Rat	1:5000 (WB)	Abcam	ab6734
Ki 67 PE Cy7 Clone B56	anti-mouse	1:100 (Flow)	BD	561283
Ki67	Rabbit	(1:200) (IF)	Abcam	ab16667
PDPN	Hamster	1:500 (IF)	Acris	DM3501
PE-CF594 CD140a Clone APA5 (RUO)	Rat anti-mouse	1:100 (Flow)	BD	562775
Perlecan AL76	Rat anti-mouse	1:100(IF)	Santa Cruz Biotechnology	sc-33707
Phospho-Ezrin(Thr567)/Radixin(Thr564)/Moesin(Thr558) (3141I)	Rabbit	1:5000 (WB)	Cell signalling technologies	3141L
Phospho-myosin light chain 2 (Ser 19)	Rabbit	1:30 (IF)	Cell signalling technologies	3671L
Podoplanin eFlour 660	Anti-mouse	1:100 (Flow)	eBioscience	50-5381-82
Zombie Aqua Fixable Viability Kit		1:1000 (Flow)	BioLegend	423102

Fig. S7. Antibody table 1